## REPORT DOCUMENTATION PAGE

READ INSTRUCTIONS BEFORE COMPLETING FORM

| | |
|---|---|
| 1. REPORT NUMBER: NRL Report 7710 | 2. GOVT ACCESSION NO. |
| 3. RECIPIENT'S CATALOG NUMBER | |
| 4. TITLE *(and Subtitle)*: Influence of Calibration Procedure Upon Determination of $J_{Ic}$ for a Titanium 6A1-4V Alloy | 5. TYPE OF REPORT & PERIOD COVERED: Final |
| | 6. PERFORMING ORG. REPORT NUMBER |
| 7. AUTHOR(s): G. R. Yoder and C. A. Griffis | 8. CONTRACT OR GRANT NUMBER(s) |
| 9. PERFORMING ORGANIZATION NAME AND ADDRESS: Naval Research Laboratory, Washington, D.C. 20375 | 10. PROGRAM ELEMENT, PROJECT, TASK AREA & WORK UNIT NUMBERS: NRL Problem M01-24, RR 022-01-46-5431 |
| 11. CONTROLLING OFFICE NAME AND ADDRESS: Department of the Navy, Office of Naval Research, Arlington, Va. 22217 | 12. REPORT DATE: April 30, 1974 |
| | 13. NUMBER OF PAGES: 26 |
| 14. MONITORING AGENCY NAME & ADDRESS*(if different from Controlling Office)* | 15. SECURITY CLASS. *(of this report)*: Unclassified |
| | 15a. DECLASSIFICATION/DOWNGRADING SCHEDULE |

16. DISTRIBUTION STATEMENT *(of this Report)*

Approved for public release; distribution unlimited

17. DISTRIBUTION STATEMENT *(of the abstract entered in Block 20, if different from Report)*

18. SUPPLEMENTARY NOTES

19. KEY WORDS *(Continue on reverse side if necessary and identify by block number)*

Compliance calibration
$J$ integral
Elastic-plastic fracture
Crack extension
Fracture
Fracture mechanics
Titanium 6A1-4V alloy

20. ABSTRACT *(Continue on reverse side if necessary and identify by block number)*

The influence of calibration procedure on the determination of $J_{Ic}$ from fatigue-precracked elastic-plastic specimens of a Ti-6A1-4V alloy has been examined. Results are compared from five compliance-type calibrations, each derived from sets of load vs load-point-displacement diagrams which differ in origin. These sets include diagrams obtained from notched specimens of two different thicknesses, diagrams generated analytically from the plane-stress and plane-strain solutions of Bucci et al. as corrected for machine

(continued)

20. Abstract (Continued)

contribution to displacement, and from the uncorrected plane-stress solution which simulates well the load vs load-point-displacement behavior of the fatigue-precracked specimens. The $J_{Ic}$ results obtained from these five calibrations are in substantial agreement with each other and with a known value of $K_{Ic}$ for this material. Preliminary results from application of the deep-slot bend approximation are in accord with those determined from the compliance-type calibration procedures.

CONTENTS

# INFLUENCE OF CALIBRATION PROCEDURE UPON DETERMINATION OF $J_{Ic}$ FOR A TITANIUM 6A1-4V ALLOY

## INTRODUCTION

A growing body of experimental evidence [1-5] supports the $J$ integral [6,7] as a criterion for the initiation of crack extension in elastic-plastic fracture. Recent $J$-integral studies have demonstrated success with an unloading, heat-tinting technique to define the critical load-point displacement associated with the initiation of crack extension ($\delta_c$) in steel [3], titanium [4], and aluminum [5] alloys. This displacement is of prime significance to the determination of $J_{Ic}$, the critical value of the $J$ integral for the initiation of crack extension in specimens of (or structures made with) materials exhibiting linear-elastic, elastic-plastic, or fully plastic load-vs-displacement behavior. In the previous report concerned with a titanium 6A1-4V alloy [4], values of $J_{Ic}$ were determined by referring $\delta_c$ to a master compliance calibration, $J(a)$ vs $\delta$, which was based on calculated loading curves which appeared to simulate well the load-vs-displacement response of elastic-plastic fatigue-precracked specimens. However there are potentially several alternative ways to obtain such a compliance calibration. Moreover other more expedient procedures for evaluation of the $J$ integral have been proposed recently which obviate the cumbersome compliance calibration technique. The purpose of this report is to compare, for this same titanium 6A1-4V alloy, values of $J_{Ic}$ inferred from different compliance calibrations as well as from one of the latter procedures, namely, the deep-slot-in-bending approximation.

Each compliance calibration requires a set of load vs displacement diagrams for specimens with different crack lengths. The different compliance calibrations to be compared have all been derived from such sets according to the method of Begley and Landes [1,2]. The calibrations differ in that their respective sets of loading diagrams vary in origin. The sets examined in this report include those generated from notched specimens of two different thicknesses, those generated analytically from plane-stress and plane-strain solutions of Bucci et al. [8] and corrected for machine contribution to displacement, and the noncorrected plane-stress solution which simulates well the load vs displacement behavior of the fatigue-precracked specimens.

To use the deep-slot bend approximation [9,10], values of the $J$ integral are determined via

$$J = \frac{2A}{Bb}, \tag{1}$$

Note: Manuscript submitted January 9, 1974.

where $A$ is the area under the load vs load-point-displacement curve relative to the displacement of interest, $B$ is specimen thickness, and $b$ is the uncracked ligament ahead of the crack tip. There is already one report of experimental confirmation of this approximation [3].

The alloy studied exhibits crack extension prior to maximum load. To determine $J_{Ic}$, values of the $J$ integral determined from a specific compliance calibration or other procedure are plotted as a function of crack extension ($\Delta a$). This extension, when taken as an average of values measured at the quarterpoints of specimen thickness, appears to be a useful parameter for defining initiation [4,5]. The initiation criterion employed in this study is that suggested recently by Paris [11] based on developmental experience with $K_{Ic}$ fracture mechanics, namely, that the crack extension

$$\Delta a_c = \frac{1}{2} \times 2\% \times 2.5 \left(\frac{K_{Ic}}{\sigma_{ys}}\right)^2, \tag{2}$$

where $K_{Ic}$ is the plane-strain fracture toughness and $\sigma_{ys}$ the yield strength. Results are considered for four types of fatigue-precracked three-point bend specimens: of two thicknesses and two crack lengths. These specimens exhibited, to varying degrees, loading behavior characteristic of the lower end of the elastic-plastic regime. That is, all exhibited limit loads which were only a fraction of those expected for the fully plastic state; further, behavior of the specimen type with the most highly constrained crack appeared to be only marginally elastic plastic, as one specimen of three of this type examined for $K_Q$ provided an ASTM-valid $K_{Ic}$ value [4].

## EXPERIMENTAL PROCEDURE

A previous report [4] provided a detailed description of the material investigated, the three-point bend tests with fatigue-precracked specimens (the results of which are to be reanalyzed in this report), the heat-tinting procedure to delineate crack extension, the measurement of $J$ using the Begley and Landes compliance-type calibration procedure, and the calculation of elastic-plastic loading curves for the compliance calibration via the solutions of Bucci et al. To recapitulate: The Ti-6A1-4V $\alpha$-$\beta$ alloy studied had a yield strength of 124 ksi (866 MPa), had an elastic modulus of $18.55 \times 10^3$ ksi (129 GPa) in the $T$ direction, and fractured by microvoid coalescence. Fatigue-precracked three-point bend specimens of $TL$ orientation (Fig. 1) were of two thicknesses, $B$ = 0.500 in. (1.27 cm) and $B$ = 1.000 in. (2.54 cm), and two nominal crack lengths, $a$ = 0.685 in. (1.74 cm) and $a$ = 0.885 in. (2.25 cm); thus there were four basic specimen types. To define the amount of crack extension for each specimen type at various points on the respective load-vs-displacement curve, duplicate specimens were loaded to successively greater displacements, unloaded, heat tinted at 600°F (589°K) for 2 hours, and subsequently broken apart. The compliance calibration procedure of Begley and Landes is outlined in Fig. 2, with which the plane-stress solution of Bucci et al. was employed to generate load vs displacement diagrams, according to

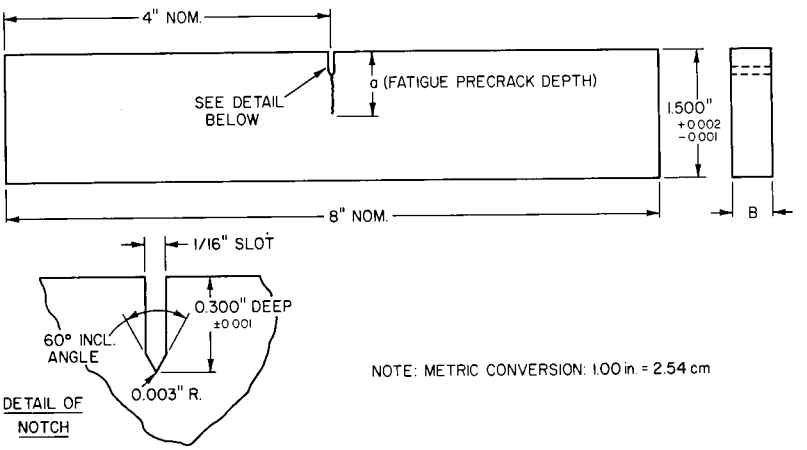


Fig. 1—Geometry of fatigue-precracked three-point bend specimens

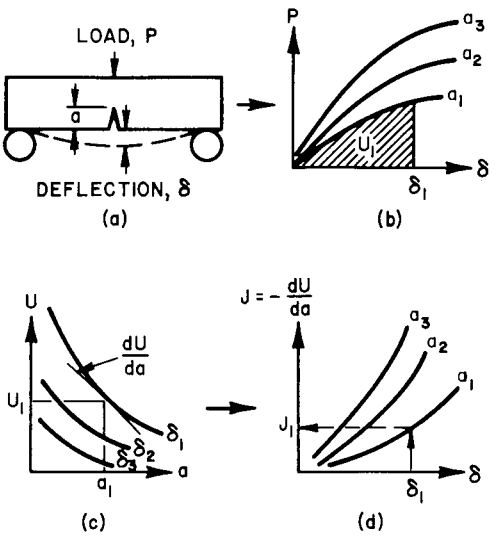


Fig. 2—Graphical method for determination of $J(a)$-vs-$\delta$ calibration: Load vs displacement response of three-point bend bars, as measured in (a), is recorded in (b) for specimens of various crack lengths $a$. Graphical integration of areas under curves in (b) gives potential energy $U$, as plotted in (c) versus crack length $a$, for various displacements $\delta$. Graphical differentiation of constant-displacement curves in (c) gives $J = -(\partial U/\partial a)_\delta$ and thus the compliance calibration curves $J(a)$ vs $\delta$ shown in (d).

$$\delta_s = \frac{0.24PS^3}{BEW^3}[1.04 + 3.28\,(W/S)^2(1+\nu)]$$

$$+ \frac{2PS^2}{BE'W^2}\left(\frac{a}{W}\right)_e\left[4.21\left(\frac{a}{W}\right)_e - 8.89\left(\frac{a}{W}\right)_e^2 + 36.9\left(\frac{a}{W}\right)_e^3\right.$$

$$- 83.6\left(\frac{a}{W}\right)_e^4 + 174.3\left(\frac{a}{W}\right)_e^5 - 284.8\left(\frac{a}{W}\right)_e^6 + 387.6\left(\frac{a}{W}\right)_e^7$$

$$\left. - 322.8\left(\frac{a}{W}\right)_e^8 + 149.8\left(\frac{a}{W}\right)_e^9\right], \qquad (3)$$

for which Poisson's ratio is taken as $\nu = 0.34$, $E' = E$, and

$$\left(\frac{a}{W}\right)_e = \frac{1}{W}\left[a + \frac{1}{\alpha\pi}\left(\frac{K}{\sigma_{ys}}\right)^2\right], \qquad (4)$$

where $\alpha = 2$* and the stress-intensity factor is given by

$$K = \frac{PS}{B(W)^{3/2}}\left[2.9\left(\frac{a}{W}\right)^{1/2} - 4.6\left(\frac{a}{W}\right)^{3/2} + 21.8\left(\frac{a}{W}\right)^{5/2} - 37.6\left(\frac{a}{W}\right)^{7/2} + 38.7\left(\frac{a}{W}\right)^{9/2}\right]. \qquad (5)$$

Using Eqs. 3 through 5, the calculated plane-stress diagrams, uncorrected for machine (loading-fixture) contribution to displacement ($\approx 4.1 \times 10^{-4}$ in./kip or $2.34 \times 10^{-4}$ cm/kN), simulated well the behavior of the fatigue-precracked specimens.

As noted in the Introduction, this report will compare results obtained with that calibration with those obtained from other compliance-type calibrations based on load vs displacement diagrams generated by machine-corrected plane-stress and plane-strain solutions of Bucci et al. as well as from loading curves of notched specimens. Two notched-specimen calibrations were made: one obtained for specimens with $B = 0.500$ in. (1.27 cm), the other with $B = 1.000$ in. (2.54 cm). In each case specimens with six notch depths were employed with $a/W$ ratios ranging from 0.3 to 0.7. A notch root radius of 0.030 in. (0.76 mm) was used in these specimens, the remaining dimensions of which conform to those of the fatigue-precracked specimens depicted in Fig. 1. The notched specimens were also tested in the same fixture, of course, as employed previously for the precracked specimens.

## RESULTS

Load-vs-displacement diagrams obtained from notched specimens appear in order of increasing $a/W$ in Figs. 3a through 3f† for specimen thickness $B = 0.500$ in. (1.27 cm).

*For plane strain $\alpha = 6$ and $E' = E/(1 - \nu^2)$.

†Plastic limit loads shown in Figs. 3 and 10 were calculated according to Refs. 8 and 12: $P_L = 1.456\,\sigma_{ts}(B/S)(W-a)^2$.

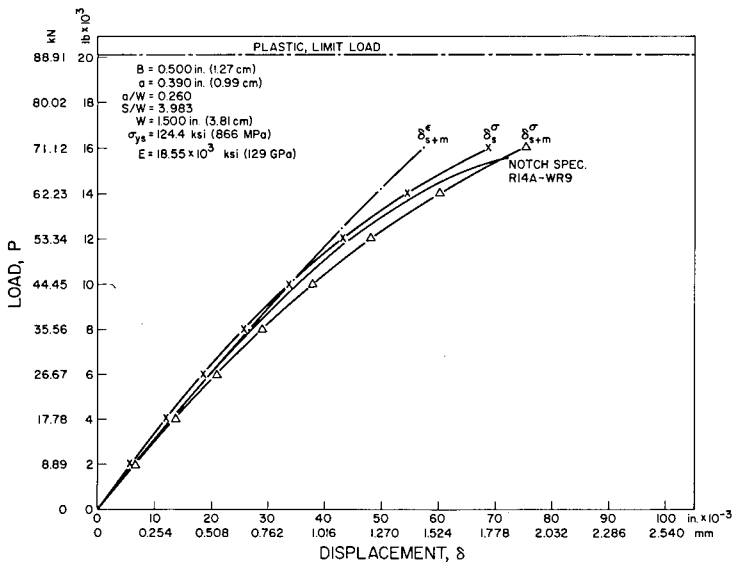


Fig. 3a—Load vs displacement diagrams from notched specimens ($B$ = 0.5 in.) for $a/W$ = 0.260. Also shown are corresponding curves obtained from machine-corrected plane-stress ($\delta^{\sigma}_{s+m}$) and plane-strain ($\delta^{\epsilon}_{s+m}$) solutions of Bucci et al. as well as uncorrected plane-stress solution ($\delta_s{}^{\sigma}$).

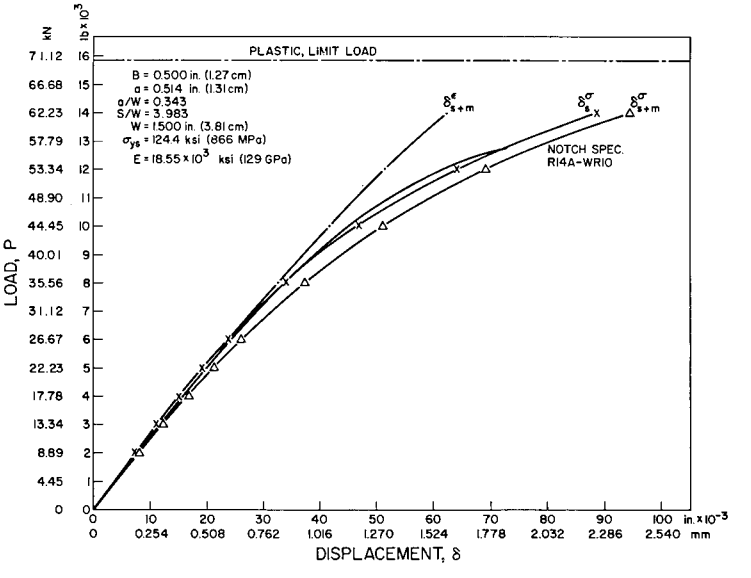


Fig. 3b—Load vs displacement diagrams from notched specimens ($B$ = 0.5 in.) for $a/W$ = 0.343. Also shown are corresponding curves obtained from machine-corrected plane-stress ($\delta^{\sigma}_{s+m}$) and plane-strain ($\delta^{\epsilon}_{s+m}$) solutions of Bucci et al. as well as uncorrected plane-stress solution ($\delta_s{}^{\sigma}$).

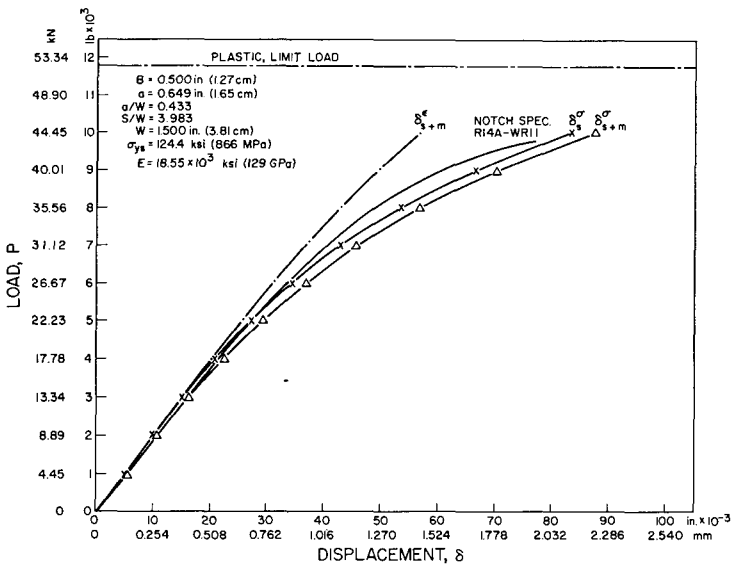


Fig. 3c—Load vs displacement diagrams from notched specimens ($B$ = 0.5 in.) for $a/W$ = 0.433. Also shown are corresponding curves obtained from machine-corrected plane-stress ($\delta^{\sigma}_{s+m}$) and plane-strain ($\delta^{\epsilon}_{s+m}$) solutions of Bucci et al. as well as uncorrected plane-stress solution ($\delta_s{}^{\sigma}$).

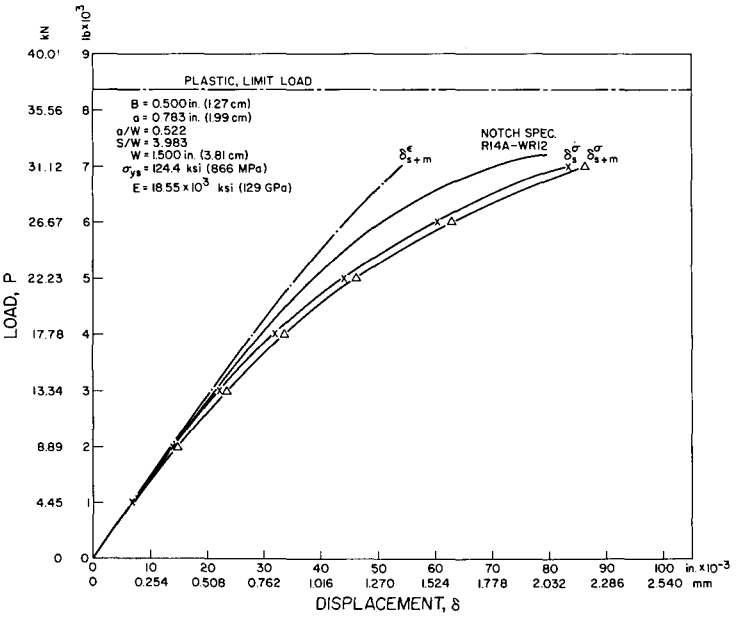


Fig. 3d—Load vs displacement diagrams from notched specimens ($B$ = 0.5 in.) for $a/W$ = 0.522. Also shown are corresponding curves obtained from machine-corrected plane-stress ($\delta^{\sigma}_{s+m}$) and plane-strain ($\delta^{\epsilon}_{s+m}$) solutions of Bucci et al. as well as uncorrected plane-stress solution ($\delta_s{}^{\sigma}$).

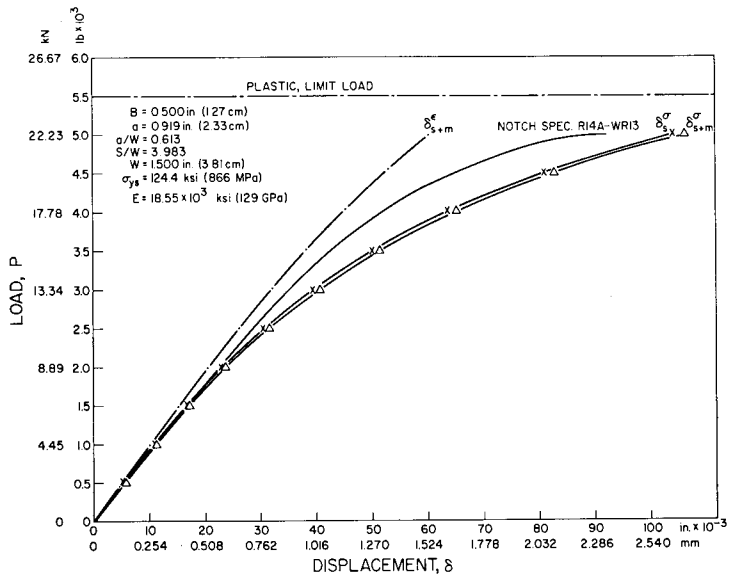


Fig. 3e—Load vs displacement diagrams from notched specimens ($B$ = 0.5 in.) for $a/W$ = 0.613. Also shown are corresponding curves obtained from machine-corrected plane-stress ($\delta^{\sigma}_{s+m}$) and plane-strain ($\delta^{\epsilon}_{s+m}$) solutions of Bucci et al. as well as uncorrected plane-stress solution ($\delta_s{}^{\sigma}$).

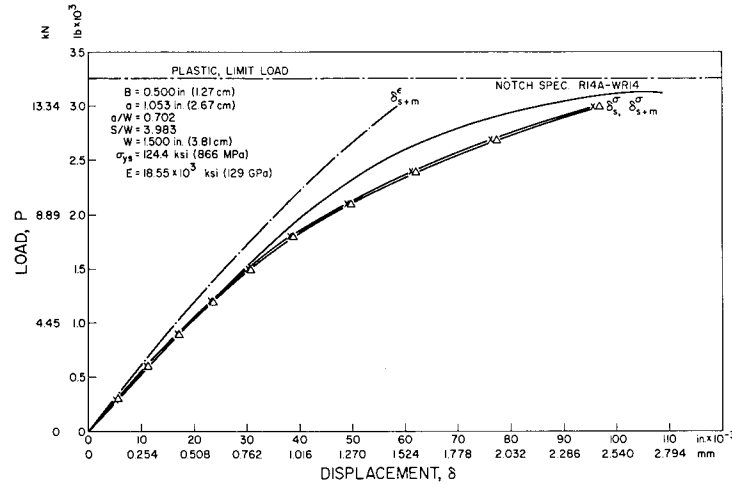


Fig. 3f—Load vs displacement diagrams from notched specimens ($B$ = 0.5 in.) for $a/W$ = 0.702. Also shown are corresponding curves obtained from machine-corrected plane-stress ($\delta^{\sigma}_{s+m}$) and plane-strain ($\delta^{\epsilon}_{s+m}$) solutions of Bucci et al. as well as uncorrected plane-stress solution ($\delta_s{}^{\sigma}$).

Also shown are the corresponding load vs displacement curves obtained from the machine-corrected plane-stress and plane-strain solutions of Bucci et al. as well as the uncorrected plane-stress solution. These latter curves are distinguished according to their respective displacement designations: $\delta^{\sigma}_{s+m}$, $\delta^{\epsilon}_{s+m}$, and $\delta_s{}^{\sigma}$.

Calibrations were formed from the different sets of loading curves. To compare values of $J_{Ic}$ as inferred from precracked-specimen results evaluated via the five calibrations, for each calibration the values of the $J$ integral are plotted versus crack extension ($\Delta a$) for all four specimen types. Results obtained using the notched-specimen calibration with $B$ = 0.5 in. are presented in Fig. 4; those from the notched-specimen calibration with $B$ = 1.0 in. are presented in Fig. 5; those from the machine-corrected plane-stress and plane-strain solutions of Bucci et al. are presented in Figs. 6 and 7 respectively, and finally those from the uncorrected plane-stress solution are presented in Fig. 8. Determinations of $J_{Ic}$ are based on a value of $\Delta a_c$ = 6 mils, according to the criterion of Eq. 2, with $K_{Ic}$ = 59.7 ksi$\sqrt{\text{in.}}$ [4]. The results in each of these figures suggest that the $J$ integral as a function of crack extension is reasonably independent of $B$ and $a$. Values of $J_{Ic}$ from the five calibrations agree well and are summarized in the upper half of Table 1 together with their translations in terms of $K_{Ic}$, assuming $J_{Ic} = K^2_{Ic}/E$. From the notched-specimen calibration with $B$ = 0.5 in., $J_{Ic}$ = 188 to 240 psi-in. ($K_{Ic}$ = 59.1 to 66.8 ksi$\sqrt{\text{in.}}$); from the notched-specimen calibration with $B$ = 1 in., $J_{Ic}$ appears to lie between 152 and 195 psi-in. ($K_{Ic}$ = 53.1 to 60.2 ksi$\sqrt{\text{in.}}$); from calibration via the plane-stress solution of Bucci et al., $J_{Ic}$ = 152 to 202 psi-in. ($K_{Ic}$ = 53.1 to 61.3 ksi$\sqrt{\text{in.}}$); from calibration via the plane strain solution of Bucci et al., $J_{Ic}$ = 155 to 223 psi-in. ($K_{Ic}$ = 53.7 to 64.4 ksi$\sqrt{\text{in.}}$), and from the loading-simulation calibration formed from the machine-uncorrected plane-stress solution of Bucci et al., $J_{Ic}$ = 188 to 242 psi-in. ($K_{Ic}$ = 59.1 to 67.0 ksi$\sqrt{\text{in.}}$).

Results from the deep-slot bend approximation are also included for comparison in Table 1. For each of the four fatigue-precracked specimen types values of $J_{Ic}$ were calculated via Eq. 2. This was accomplished by first obtaining the critical displacement corresponding to $\Delta a_c$ = 6 mils from Fig. 9, where displacement is plotted as a function of crack extension. Then the integrated areas under the respective load vs displacement traces up to the critical displacement, minus the machine contribution of the testing fixture, are employed in Eq. 2 for the calculation. The four calculations provide estimates of $J_{Ic}$ = 202, 167, 195, and 211 psi-in., which translate via $J_{Ic} = K^2_{Ic}/E$ to $K_{Ic}$ = 61.3, 55.7, 60.2, and 62.6 ksi$\sqrt{\text{in.}}$ respectively. These values are well within the bounds for $J_{Ic}$ defined from the compliance-type calibrations.

## DISCUSSION

Results from the comparative study of compliance-type calibrations suggest that load vs displacement diagrams of quite diverse origins may be employed to generate calibrations $J(a)$ vs $\delta$, which yield substantially equivalent results in the evaluation of $J_{Ic}$ from fatigue-precracked specimens. Divergence of the analytically generated loading diagrams relative to those of the respective precracked specimens is illustrated in Figs. 10a through 10d for the four precracked specimen types. For one type (Fig. 10a) the behavior of a notched specimen with notch depth equal to the length of the crack in the fatigue-precracked specimen is also compared; a sizeable difference is evident. Thus it is

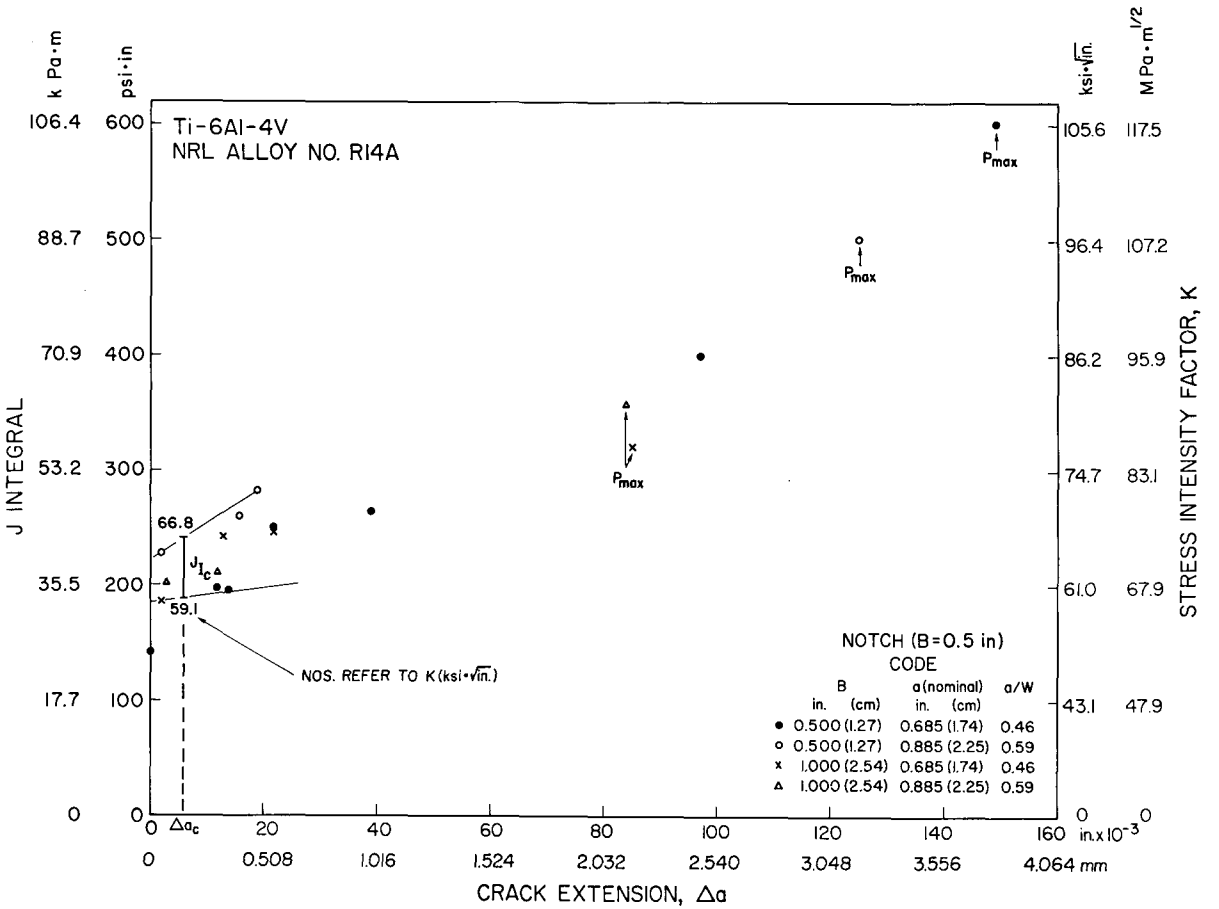


Fig. 4—Determination of $J_{Ic}$ using the notched-specimen calibration with $B$ = 0.5 in.

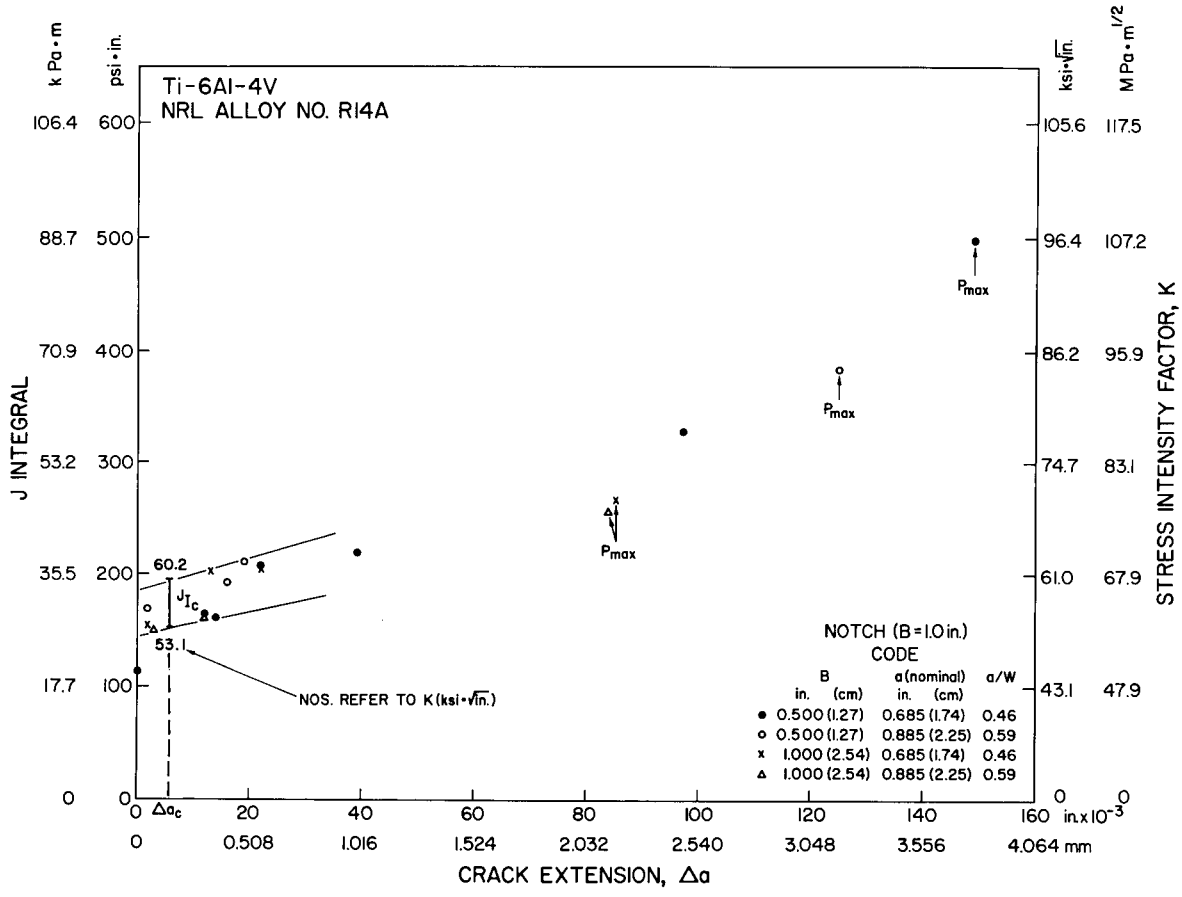


Fig. 5—Determination of $J_{Ic}$ using the notched-specimen calibration with $B$ = 1.0 in.

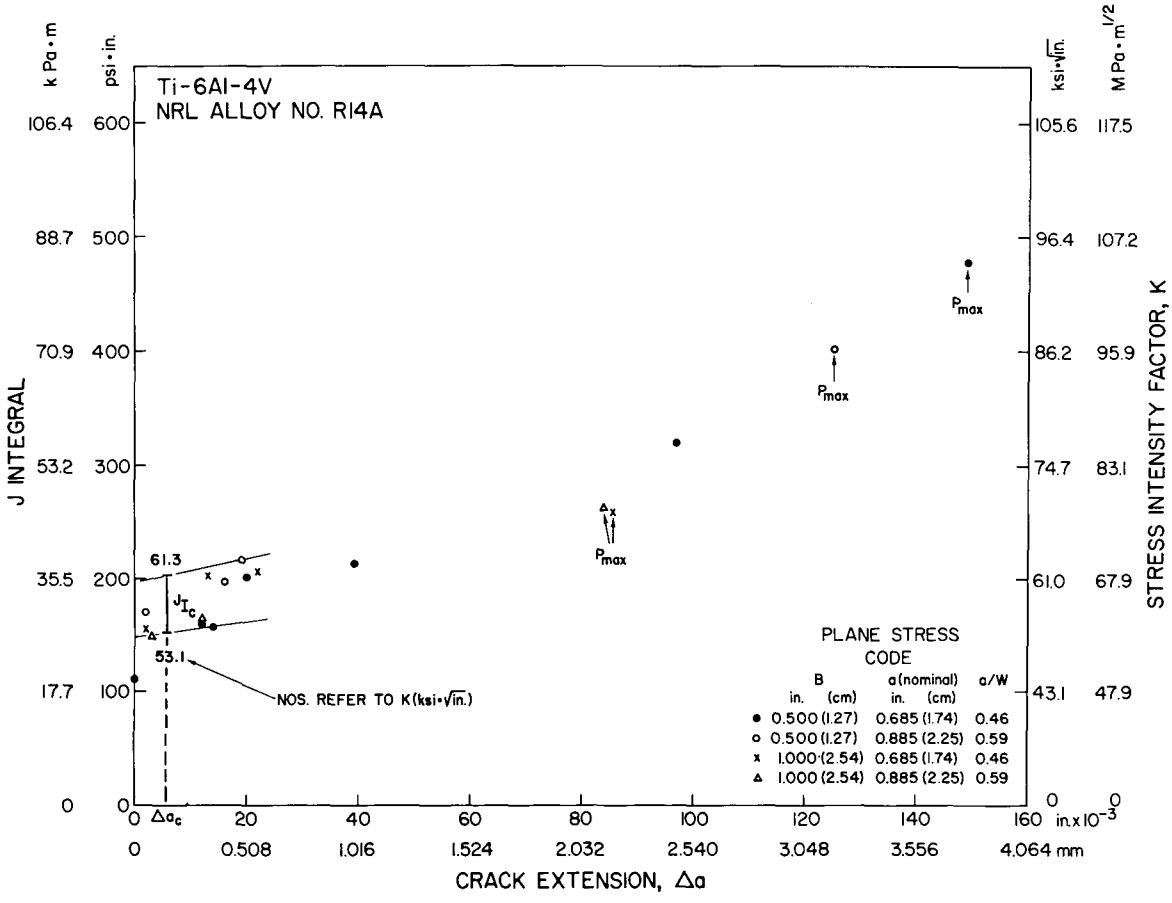


Fig. 6—Determination of $J_{Ic}$ using the calibration from the machine-corrected plane-stress solution of Bucci et al.

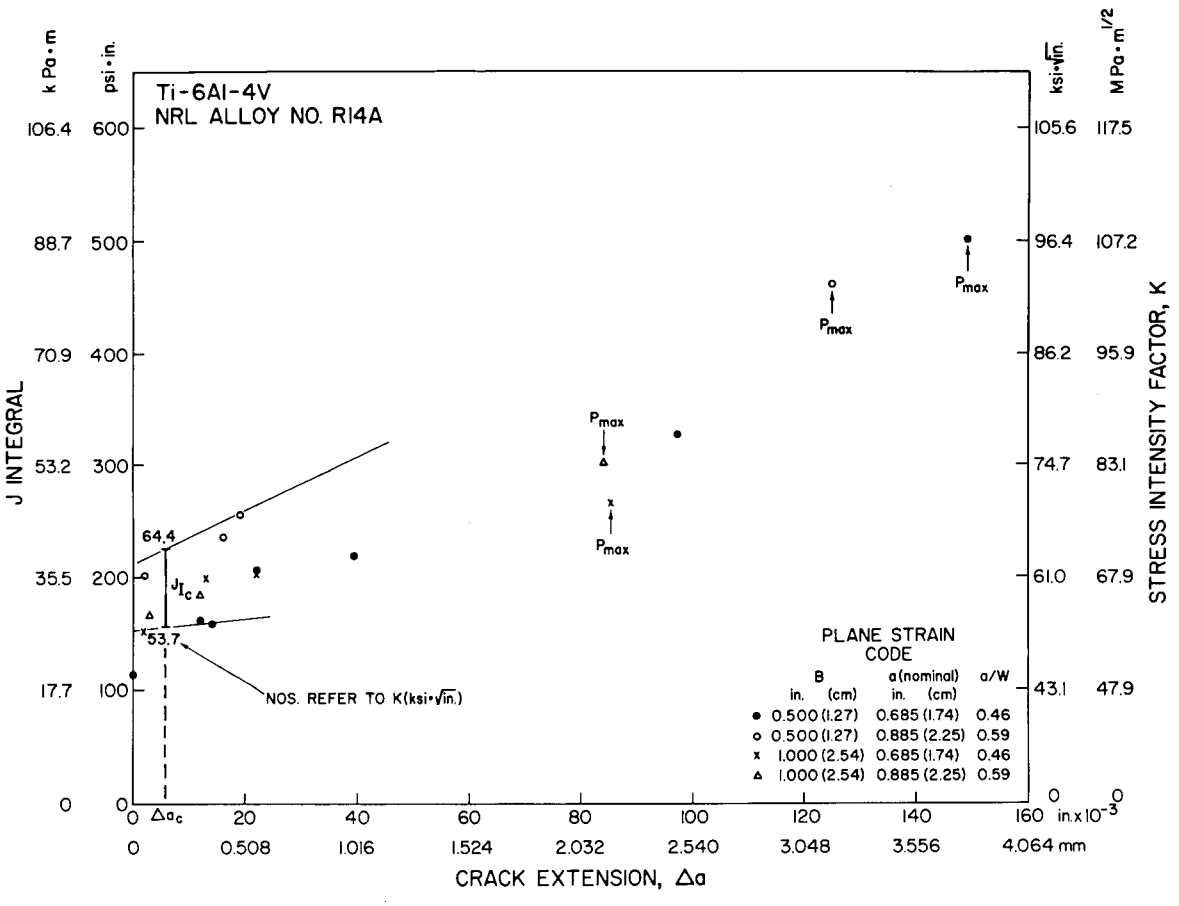


Fig. 7—Determination of $J_{Ic}$ using the calibration from the machine-corrected plane-strain solution of Bucci et al.

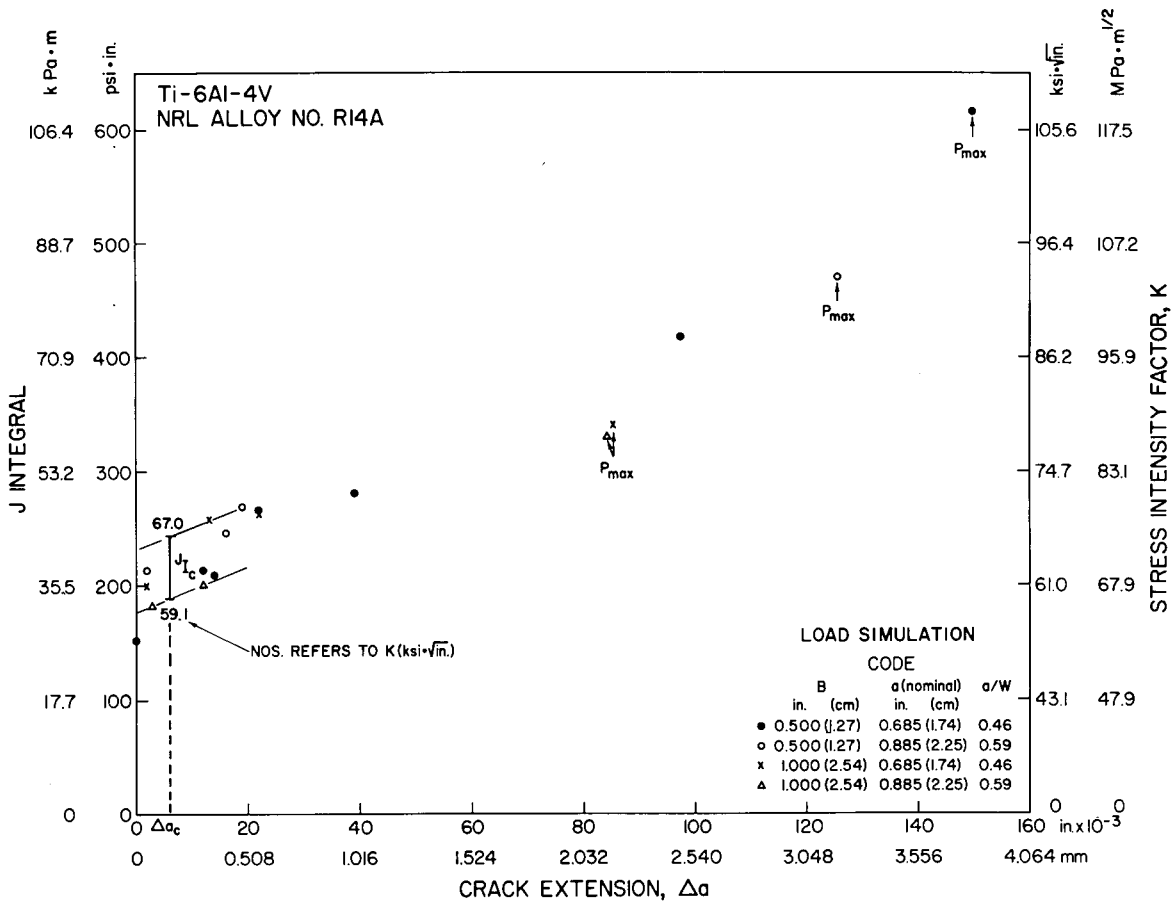


Fig. 8—Determination of $J_{Ic}$ using the calibration from the machine-uncorrected plane-stress solution of Bucci et al. (loading simulation)

Table 1
Effect of the Calibration Procedure on the $J_{Ic}$ Determination

| Calibration Type or (for the Deep-Slot Bend Approximation) Specimen Type | $J_{Ic}$ (psi-in.)* | | $K_{Ic}$ (ksi$\sqrt{\text{in.}}$)† | |
|---|---|---|---|---|
| | Max | Min | Max | Min |
| Notch ($B$ = 1.0 in.) | 195 | 152 | 60.2 | 53.1 |
| Notch ($B$ = 0.5 in.) | 240 | 188 | 66.8 | 59.1 |
| Plane stress | 202 | 152 | 61.3 | 53.1 |
| Plane strain | 223 | 155 | 64.4 | 53.7 |
| Loading simulation | 242 | 188 | 67.0 | 59.1 |
| Deep-Slot Bend Approximation (for Comparison) | | | | |
| $B$ = 1.0 in., $a/W$ = 0.46 | 202 | | 61.3 | |
| $B$ = 1.0 in., $a/W$ = 0.59 | 167 | | 55.7 | |
| $B$ = 0.5 in., $a/W$ = 0.46 | 195 | | 60.2 | |
| $B$ = 0.5 in., $a/W$ = 0.59 | 211 | | 62.6 | |

*1 psi-in. = 177.3 Pa-m.
†1 ksi$\sqrt{\text{in.}}$ = 1.112 MPa-m$^{1/2}$.

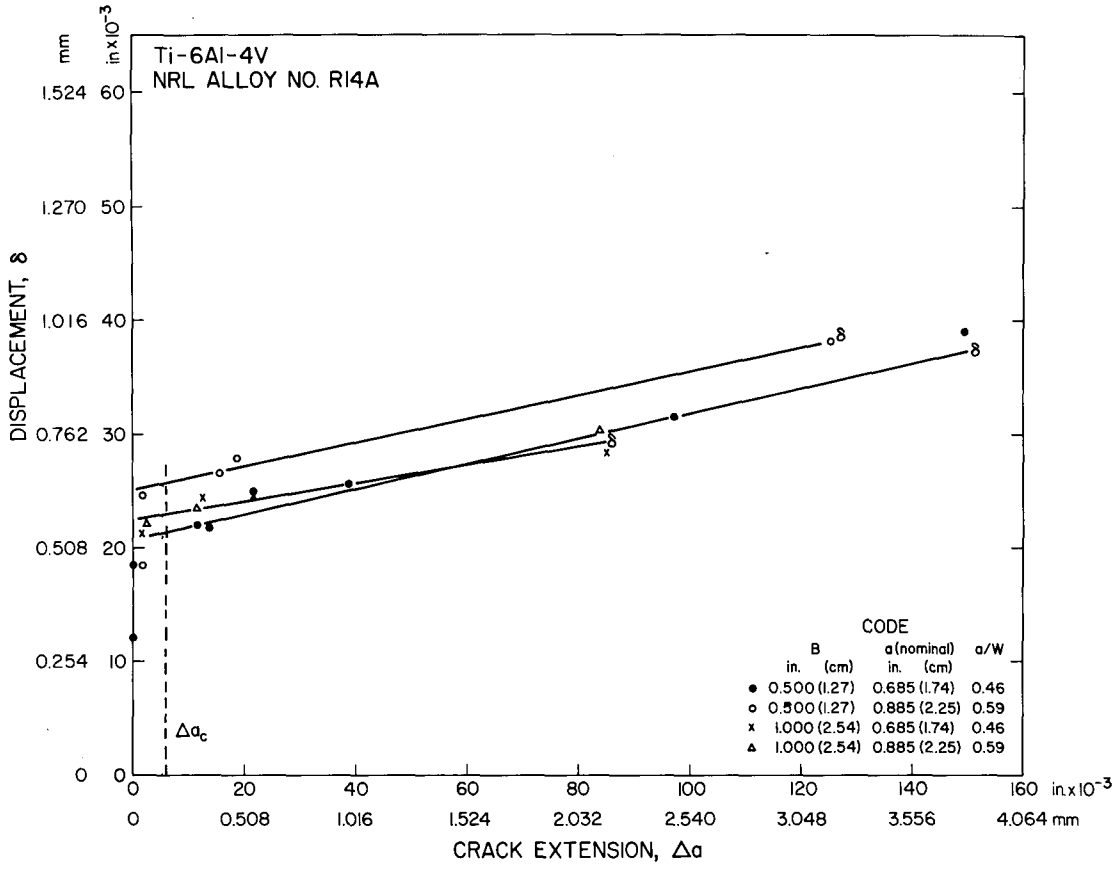


Fig. 9—Load-point displacement ($\delta$) as a function of crack extension ($\Delta a$) in fatigue-precracked specimens [4]

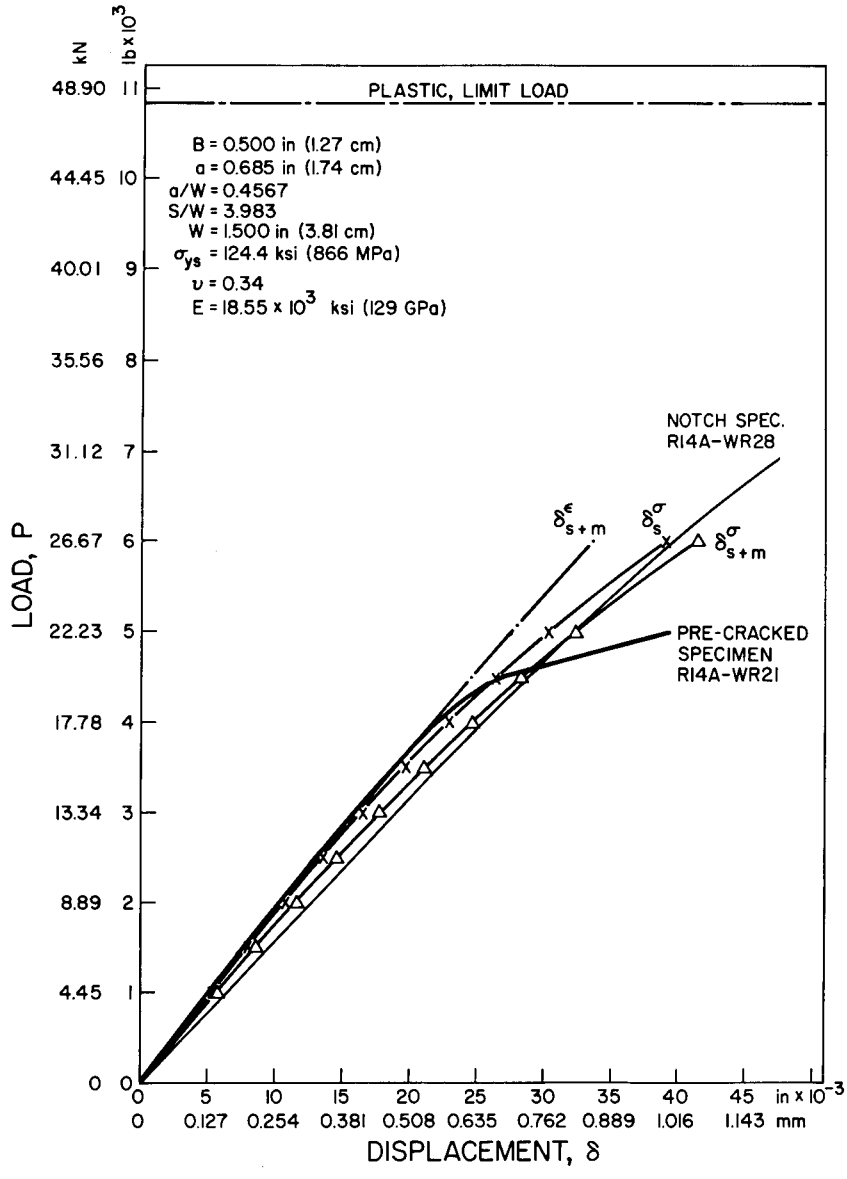


Fig. 10a—Comparison of analytically generated loading diagrams to that of the fatigue-precracked specimen with $B = 0.500$ in. and $a = 0.685$ in. Notched-specimen behavior is also shown.

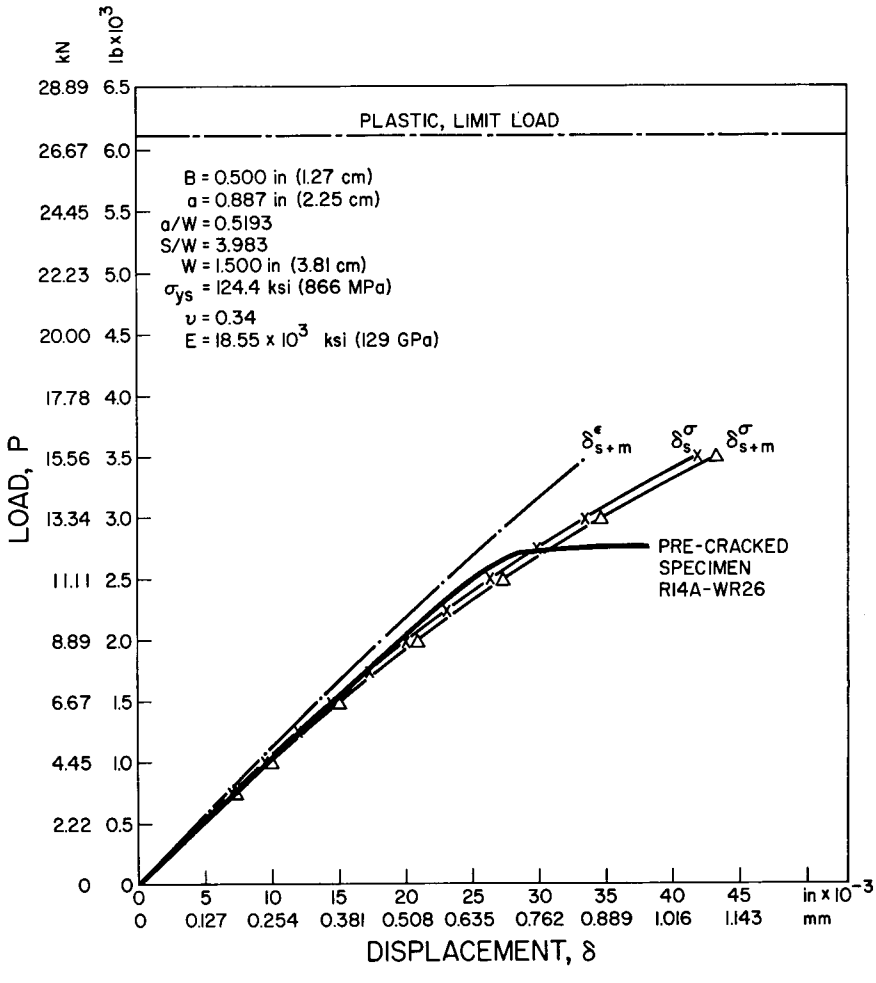


Fig. 10b—Comparison of analytically generated loading diagrams to that of the fatigue-precracked specimen with $B$ = 0.500 in. and $a$ = 0.887 in.

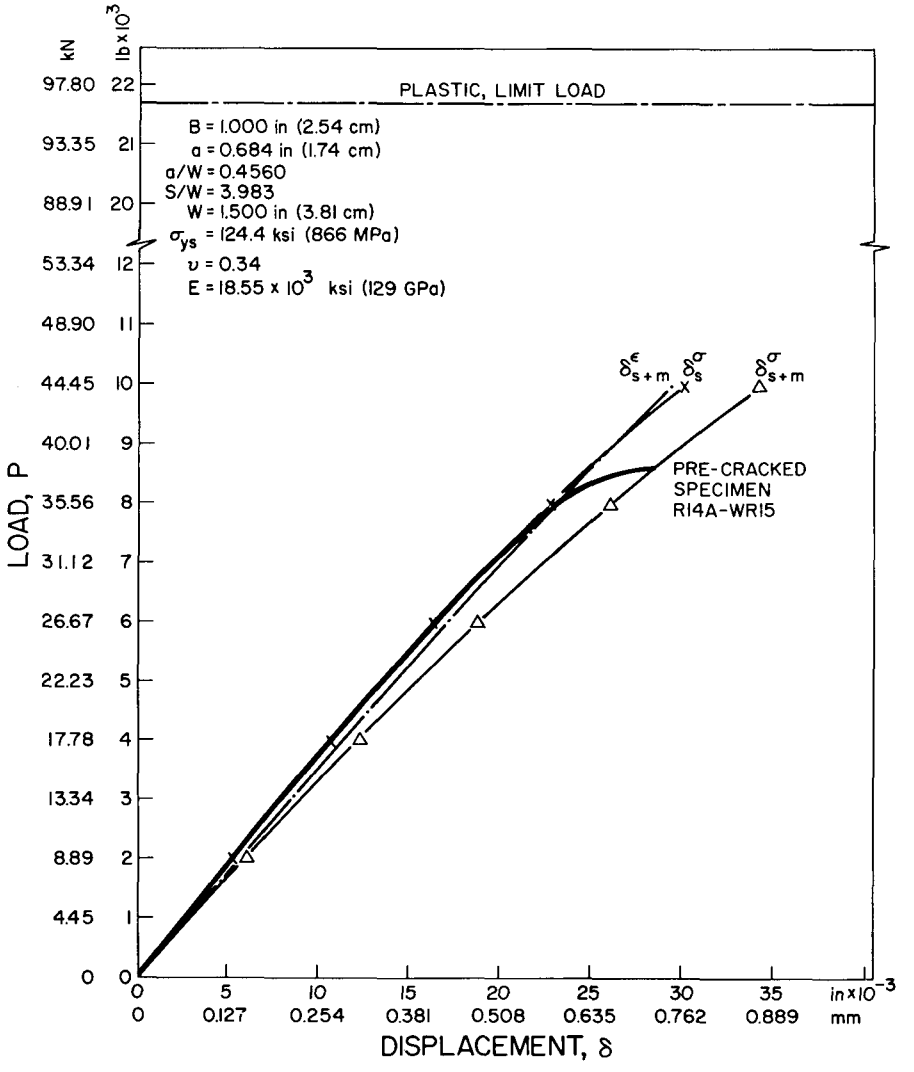


Fig. 10c—Comparison of analytically generated loading diagrams to that of the fatigue-precracked specimen with $B$ = 1.000 in. and $a$ = 0.684 in.

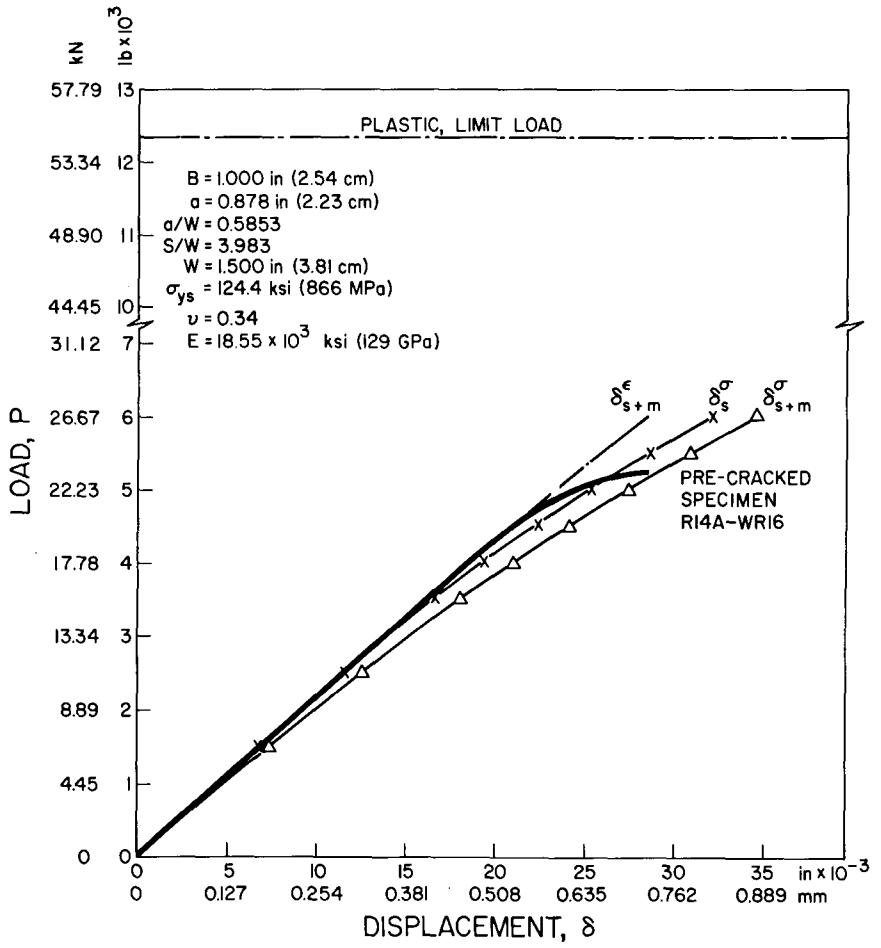


Fig. 10d—Comparison of analytically generated loading diagrams to that of the fatigue-precracked specimen with $B$ = 1.000 in. and $a$ = 0.878 in.

apparent that precise simulation of load vs displacement diagrams of precracked specimens is not necessary for calibration purposes, as it is the change in load vs displacement behavior with crack length that would be expected to be of prime importance [6,8,13].

While the degree of uncertainty in $J_{Ic}$ as determined with each calibration may be somewhat greater than desired for precise comparison of the five, the degree of scatter is no greater than the toughness variation which would be expected in the plate itself [14]. It might also be noted that some of the calibrations infer $J_{Ic}$ levels a shade higher or lower than others. These differences are relatively small however; they are of the same order as the uncertainty in translation of the ASTM-valid $K_{Ic}$ value for this material (59.7 ksi$\sqrt{\text{in.}}$) to $J_{Ic}$ itself [13,15,16]: $J_{Ic}$ = 170 psi-in. if $J = K^2(1 - \nu^2)/E$ is assumed vs $J_{Ic}$ = 192 psi-in. if $J = K^2/E$ is assumed. Furthermore the quoted $K_{Ic}$ value may be lower than the average value of the plate material, inasmuch as two out of three $K_Q$ tests with identical specimens failed to provide a valid $K_{Ic}$ determination via ASTM-E399-72 [4]. In view of these uncertainties it is difficult to conclude that any one of the calibrations is superior to the others.

## SUMMARY

The influence of calibration procedure on the determination of $J_{Ic}$ from fatigue-precracked elastic-plastic specimens of a Ti-6A1-4V alloy has been studied. Results are compared from five compliance-type calibrations, each derived from sets of load vs displacement diagrams according to the method of Begley and Landes. The calibrations differ as to the origin of the sets of loading diagrams. The sets examined in this work include those generated from notched specimens of two different thicknesses and those generated analytically from plane-stress and plane-strain solutions of Bucci et al. as corrected for machine contribution to displacement and from the noncorrected plane-stress solution which simulates well the load vs displacement behavior of the fatigue-precracked specimens. The $J_{Ic}$ results obtained from these five calibrations are in substantial agreement with each other and with a known value of $K_{Ic}$ for this material.

Preliminary results from application of the deep-slot bend approximation are in good agreement with those determined by the compliance-type calibration procedures compared in this report.

## ACKNOWLEDGMENTS

The authors gratefully acknowledge Mr. S. J. McKaye for able technical assistance and the office of Naval Research for financial support. Special thanks are extended to Drs. G. R. Irwin and F. J. Loss for stimulating discussions during the evolution of this work.

## REFERENCES


1. J. A. Begley and J. D. Landes, "The *J* Integral as a Fracture Criterion," pp. 1-20 in *Fracture Toughness*, Proc. 1971 Nat. Symp. on Frac. Mech., Part II, ASTM STP 514, Am. Soc. Testing Mat., Philadelphia, 1972.
2. J. D. Landes and J. A. Begley, "The Effect of Specimen Geometry on $J_{Ic}$," pp. 24-39 in *Fracture Toughness*, Proc. 1971 Nat. Symp. on Frac. Mech., Part II, ASTM STP 514, Am. Soc. Testing Mat., Philadelphia, 1972.
3. J. D. Landes and J. A. Begley, "Test Results from *J* Integral Studies—An Attempt to Establish a $J_{Ic}$ Testing Procedure," presented at 7th National Symposium on Fracture Mechanics, 28 Aug. 1973, University of Maryland; also at meeting of *J* Integral Task Group (No. TG-E24.01.09), Committee E24 on Fracture Testing of Metals, ASTM, 10 Oct. 1973, Pittsburgh, to be published by ASTM, Philadelphia.
4. G. R. Yoder and C. A. Griffis, "*J* Integral and the Initiation of Crack Extension in a Titanium Alloy," NRL Report 7662, February 26, 1974.
5. C. A. Griffis and G. R. Yoder, "Application of the *J* Integral to Crack Initiation in a 2024-T351 Aluminum Alloy," NRL Report 7676, April 3, 1974.
6. J. R. Rice, "A Path Independent Integral and the Approximate Analysis of Strain Concentration by Notches and Cracks," Trans. ASME, Series E, J. Applied Mechanics 35 (1968) 379-386.
7. J. R. Rice, "Mathematical Analysis in the Mechanics of Fracture," Chapter 3 in *Fracture*, Vol. II, H. Liebowitz, editor, Academic Press, New York, 1968, pp. 191-311.
8. R. J. Bucci, P. C. Paris, J. D. Landes, and J. R. Rice, "*J* Integral Estimation Procedures," pp. 40-69 in *Fracture Toughness*, Proc. 1971 Nat. Symp. on Frac. Mech., Part II, ASTM STP 514, Am. Soc. Testing Mat., Philadelphia, 1972.
9. J. R. Rice, P. C. Paris, and J. G. Merkle, "Some Further Results of *J* Integral Analysis and Estimates," pp. 231-245 in *Progress in Flaw Growth and Fracture Toughness Testing*, ASTM STP 536, Am. Soc. Testing Mat., Philadelphia, 1973.
10. J. E. Srawley, "On the Rice *J* Integral Concept in Fracture Mechanics," lecture notes, NASA Lewis Research Center, Cleveland, July 1972; also footnote 6 on p. 235 in Ref. 9.
11. P. C. Paris, discussion presented at meeting of *J* Integral Task Group (No. TG-E24.01.09), Committee E24 on Fracture Testing of Metals, ASTM, 10 Oct. 1973, Carnegie-Mellon University, Pittsburgh.
12. A. P. Green and B. B. Hundy, "Initial Plastic Yielding in Notch Bend Tests," J. of the Mech. and Phys. of Solids 4 (1956) 128-144.
13. J. E. Srawley, "Plane Strain Fracture Toughness," Chapter 2 in *Fracture*, Vol. IV, H. Liebowitz, editor, Academic Press, New York, 1969, pp. 45-68.
14. R. J. Goode, Naval Research Laboratory, personal communication, 1973.

15. G. R. Irwin, written discussion to Ref. 1, pp. 22-23 in *Fracture Toughness*, Proc. 1971 Nat. Symp. on Fr. Mech., Part II, ASTM STP 514, Am. Soc. Testing Mat., Philadelphia, 1972.

16. G. R. Irwin, and P. C. Paris, "Fundamental Aspects of Crack Growth and Fracture, Chapter 1 in *Fracture*, Vol. III, H. Liebowitz, editor, Academic Press, New York, 1971, pp. 1-46.

## NOMENCLATURE

$A$ = integrated area under a load vs load-point-displacement curve

$a$ = crack length

$\Delta a$ = crack extension

$\Delta a_c$ = crack extension used to define the initiation of crack extension

$B$ = thickness of the specimen

$b$ = uncracked ligament, $W - a$

$E$ = Young's modulus

$J$ = value of the $J$ integral

$J_{Ic}$ = critical value of the $J$ integral for the initiation of crack extension

$K$ = stress-intensity factor

$K_{Ic}$ = critical value of the stress-intensity factor for initiation of crack extension

$K_Q$ = stress-intensity factor defined by ASTM-E399-72 5-percent secant-offset method, from record of load vs crack-mouth-opening deflection

$P$ = applied load

$P_{max}$ = maximum load

$S$ = span length in three-point bend test

$U$ = potential energy per unit thickness

$W$ = depth of specimen

$\delta$ = load-point displacement

$\delta_c$ = critical load-point displacement for the initiation of crack extension defined by $\Delta a_c$

$\delta_s$ = load-point displacement owing to the specimen alone

$\delta_s^{\sigma}$ = $\delta_s$ obtained from the plane-stress solution of Bucci et al.

$\delta_{s+m}^{\sigma}$ = $\delta_s^{\sigma}$ corrected for the machine contribution to $\delta$

$\delta_{s+m}^{\epsilon}$ = $\delta_s$ obtained from the plane-strain solution of Bucci et al. corrected for the machine contribution to $\delta$

$\nu$ = Poisson's ratio

$\sigma_{ts}$ = uniaxial tensile strength

$\sigma_{ys}$ = yield stress


NRL7721

SECURITY CLASSIFICATION OF THIS PAGE *(When Data Entered)*

## REPORT DOCUMENTATION PAGE

READ INSTRUCTIONS BEFORE COMPLETING FORM

| | |
|---|---|
| 1. REPORT NUMBER: NRL Report 7721 | 2. GOVT ACCESSION NO. |
| 3. RECIPIENT'S CATALOG NUMBER | |
| 4. TITLE *(and Subtitle)*: THE EFFECT OF STRAY DIRECT CURRENT AT VARIOUS CURRENT DENSITIES ON THE CORROSION OF STEEL | 5. TYPE OF REPORT & PERIOD COVERED: Final report on one phase of a continuing NRL Problem. |
| | 6. PERFORMING ORG. REPORT NUMBER |
| 7. AUTHOR(s): T. J. Lennox, Jr. and M. H. Peterson | 8. CONTRACT OR GRANT NUMBER(s) |
| 9. PERFORMING ORGANIZATION NAME AND ADDRESS: Naval Research Laboratory, Washington, D.C. 20375 | 10. PROGRAM ELEMENT, PROJECT, TASK AREA & WORK UNIT NUMBERS: NRL Problem M04-02, SF 51-542-602-12431, RR 022-08-44-5510 |
| 11. CONTROLLING OFFICE NAME AND ADDRESS: Department of the Navy, Office of Naval Research, Arlington, Virginia 22217 | 12. REPORT DATE: April 4, 1974 |
| | 13. NUMBER OF PAGES: 22 |
| 14. MONITORING AGENCY NAME & ADDRESS*(if different from Controlling Office)* | 15. SECURITY CLASS. *(of this report)*: Unclassified |
| | 15a. DECLASSIFICATION/DOWNGRADING SCHEDULE |

16. DISTRIBUTION STATEMENT *(of this Report)*

Approved for public release; distribution unlimited.

17. DISTRIBUTION STATEMENT *(of the abstract entered in Block 20, if different from Report)*

18. SUPPLEMENTARY NOTES

19. KEY WORDS *(Continue on reverse side if necessary and identify by block number)*

Stray direct current on steel ships
0.6M (3.5%) NaCl solution
Electrode potentials and IR drop
Intermediate electrode (bipolar anode and bipolar cathode) (Continues)

20. ABSTRACT *(Continue on reverse side if necessary and identify by block number)*

Stray current corrosion has been of major concern to the Navy over the past few years. Serious corrosion attributable to stray current has occurred in seawater or brackish water on several occasions where the possibility of the corrosion being from improper welding was precluded. The experimental technique used isolates the bipolar anodes and bipolar cathodes so that stray current corrosion parameters can be studied and quantized. Data are presented on the effect of various stray dc densities on the corrosion rates and the electrode potentials of

(Continues)

DD FORM 1 JAN 73 1473 EDITION OF 1 NOV 65 IS OBSOLETE
S/N 0102-014-6601 |



SECURITY CLASSIFICATION OF THIS PAGE *(When Data Entered)*

19.

Current density, effect, on steel
Theoretical metal-loss rate
Corrosion rate
Corrosion characteristics

20.

steel both as common electrodes and as bipolar (or intermediate) electrodes. The metal-loss rates have also been compared to the theoretical values based on the reaction $Fe-2e=Fe^{+2}$.

The mean dissolution potential for steel in 0.6M (3.5%) NaCl solution was approximately −0.7 V to the Ag/AgCl reference electrode, and was essentially independent of the current density. Similar values were observed for anodes, bipolar anodes and freely corroding control specimens. Steel could not be polarized cathodically to a mean potential more negative than −1.015 volts to the Ag/AgCl reference electrode. Mean potentials either more positive than −0.7 V or more negative than −1.015 V were observed only when the measurement included an IR drop.

Potential measurement can be used to detect stray current on steel only at relatively high current densities. The corrosion characteristics of steel anodes and bipolar anodes were similar at any one current density, but varied with current density.

CONTENTS

# THE EFFECT OF STRAY DIRECT CURRENT AT VARIOUS CURRENT DENSITIES ON THE CORROSION OF STEEL

## INTRODUCTION

There have been several incidences of very severe corrosion on naval ship hulls in the past few years. In at least some of these cases, the possibility of the corrosion being caused by improper welding techniques has been eliminated. Field studies have been made in which the recorded hull potential intermittently showed large fluctuation in the positive direction indicating that stray currents do exist at some naval berthing sites. The source of these stray currents, however, was not established.

As part of a continuing effort to gain further insight into stray current corrosion and mitigation, personnel of the Naval Research Laboratory have been conducting laboratory experiments to quantify the corrosion caused by stray currents. Parameters that may be useful in stray current detection are also being studied.

Stray electrical currents can flow through multiple paths which generally result in a very complex network. For stray direct currents on steel, the primary concern is the corrosion at the anodes and bipolar (or intermediate) anodes.

A bipolar or intermediate electrode exists when a metal, other than the primary anode and cathode, is in an electrolytic cell and the metal has no metallic contact with the current source or return to the source, i.e., the metal is an electrically isolated, floating electrode. A ship in an electrical direct-current field is a bipolar or intermediate electrode if it is not metallically connected to the source or return for the current. Figure 1 shows a ship (Ship 2) in a stray-current field as a bipolar or intermediate electrode. This ship would receive current at one location on the hull and discharge current into the water from some other area on the hull. The location where the current leaves the hull would be a bipolar anode and would corrode at an accelerated rate.

The location on the steel hull where the current was received from the solution would be a bipolar or intermediate cathode. There should be no concern about accelerated corrosion of steel bipolar cathodes because at these points the steel would receive at least partial cathodic protection. The electrochemical reactions at the bipolar cathode should also produce an alkaline condition which would tend to further reduce the corrosion of the steel. Similar to intentional cathodic protection, the possibility of hydrogen embrittlement on susceptible steels and hydrogen discharge into a confined space would be of concern.

This report presents data obtained on low-carbon steel in stray direct-current fields of various intensities. In order to minimize variables, these studies were conducted on

Manuscript submitted January 22, 1974.

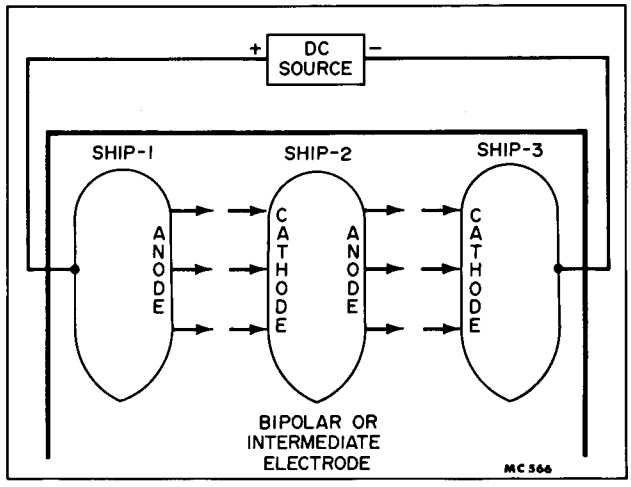


Fig. 1 — Stray currents and bipolar or intermediate electrodes

laboratory scale models. The solution used in all experiments was 0.6M (3.5%) NaCl in tap water with a resistivity of 19 ohm-cm.

## EXPERIMENTAL TECHNIQUE

A planar bipolar electrode would pick up current on one side (or surface) and discharge the current into the water from the opposite side. To quantify stray-current corrosion parameters, it is necessary to have two separate metal specimens to simulate a bipolar electrode; one specimen being the bipolar cathode and the second the bipolar anode. These experiments were designed so that quantitative data could be obtained on anodes, bipolar anodes, cathodes, and bipolar cathodes.

Individualizing the bipolar cathode and the bipolar anode was achieved by the experimental technique shown in Fig. 2. An anode and bipolar cathode were positioned in one acrylic tank and a bipolar anode and cathode were in a second acrylic tank. The anode and cathode were electrically connected to the direct-current power source. The bipolar cathode and the bipolar anode were electrically connected to each other, but were not electrically connected to the power source or to the metallic return to the power source. An electrically isolated, floating, bipolar electrode was thus obtained, and each half of the bipolar electrode could be studied independently. Each electrode measured 6X8X1/32 in. The cross section of the tank was 6X8 in. and the internal length of the acrylic tanks was approximately 21 in. The cross section of the solution in the tank was 6 X 6 3/4 in. The electrodes were positioned at the extreme ends of the tanks. A constant area of each specimen was in contact with the solution so the apparent current density could be controlled at selected levels.

The area of metal exposed to the solution was 26.25 sq in., i.e., 5X5-1/4 in. on the one flat surface of each specimen facing the bulk solution. The other areas on the specimens were masked with 15-mil-thick vinyl tape. The masking also served to eliminate possible

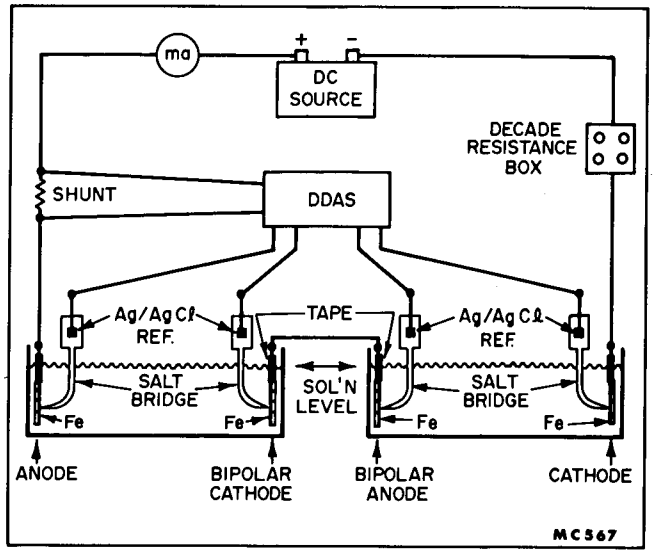


Fig. 2 — Stray current experimental technique

edge and water line effects. Each specimen was weighed to 0.01 g before and after the experiment to permit metal-loss rates (corrosion rates) to be calculated.

The potential of each specimen was measured relative to a Ag/AgCl reference electrode. The Ag/AgCl reference electrodes were located in inverted polyethylene bottles to which a polystyrene capillary tube was attached. The plastic bottle and capillary were filled with 0.6M (3.5%) NaCl solution, and served as a salt bridge from the Ag/AgCl reference electrode to the specimen. The tip of the capillary was positioned essentially in contact with the metal electrodes being studied in order to eliminate as much voltage (IR) drop from the potential measurement as possible.

The time between potential measurements was programmed and the potentials were recorded on a Digital Data Acquisition System (DDAS). The potentials were measured both with the current on and the current off. The current-off potentials were obtained by manually interrupting the electrical current flow in the system for less than 5 s. The current-off potentials completely excluded the IR drop from the potential measurements and therefore are better values for the potential at the metal surfaces.

The source of the direct current was a 12-V lead-acid storage battery. A milliammeter in the circuit indicated the current flow and the current was recorded on the DDAS by measuring the potential drop across a precision resistor (shunt). The current was controlled at preselected levels by a decade resistance box in series in the circuit.

At the conclusion of each experiment, the tape used for masking the selected areas was removed from the specimens and the electrodes were cleaned with ethyl alcohol to remove any remaining adhesive. Prior to the final weighing, the specimens were cleaned at room temperature by brushing in HCl containing 40 g/l of $Sb_2O_3$; rinsed in distilled water; and dried with ethyl alcohol and a jet of dry nitrogen gas.

## DATA AND DISCUSSION

### Electrode Potentials vs Time

Figures 3 — 6 show the potential vs time data for steel at direct-current densities of 5, 10, 100 and 1000 mA per square foot (mA/sq ft), respectively, after an initial stabilization period of approximately 1 hr. The potentials of freely corroding steel are shown for the entire time periods. At the three highest current densities, the same range of potentials has been used on the ordinate axis, i.e., —0.3 to —1.3 V to the Ag/AgCl reference electrode.

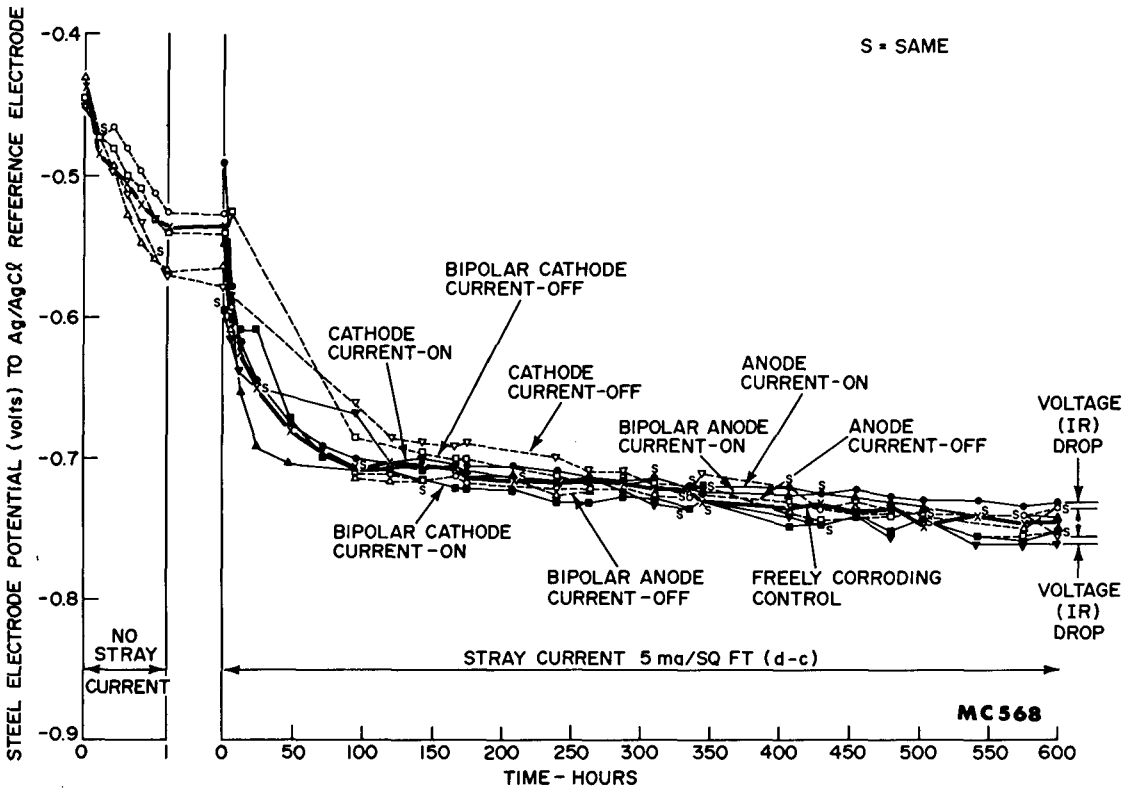


Fig. 3 — The effect of stray direct current on steel electrodes in 0.6M (3.5%) NaCl solution. Potential vs time data at a current density of 5 mA/sq ft.

For a current density of 5 mA/sq ft, the ordinate axis covers the potential range from —0.4 to —0.9 V. The same time scale has been used for the abscissa at all the current densities except for the data at a current density of 1000 mA/sq ft, where an expanded time scale has been used because the experiment at this current density lasted only 48 hrs.

Figure 3 shows that at a stray direct-current (dc) density of 5 mA/sq ft or less it would not be possible to detect stray currents by measuring the potentials of the electrodes.

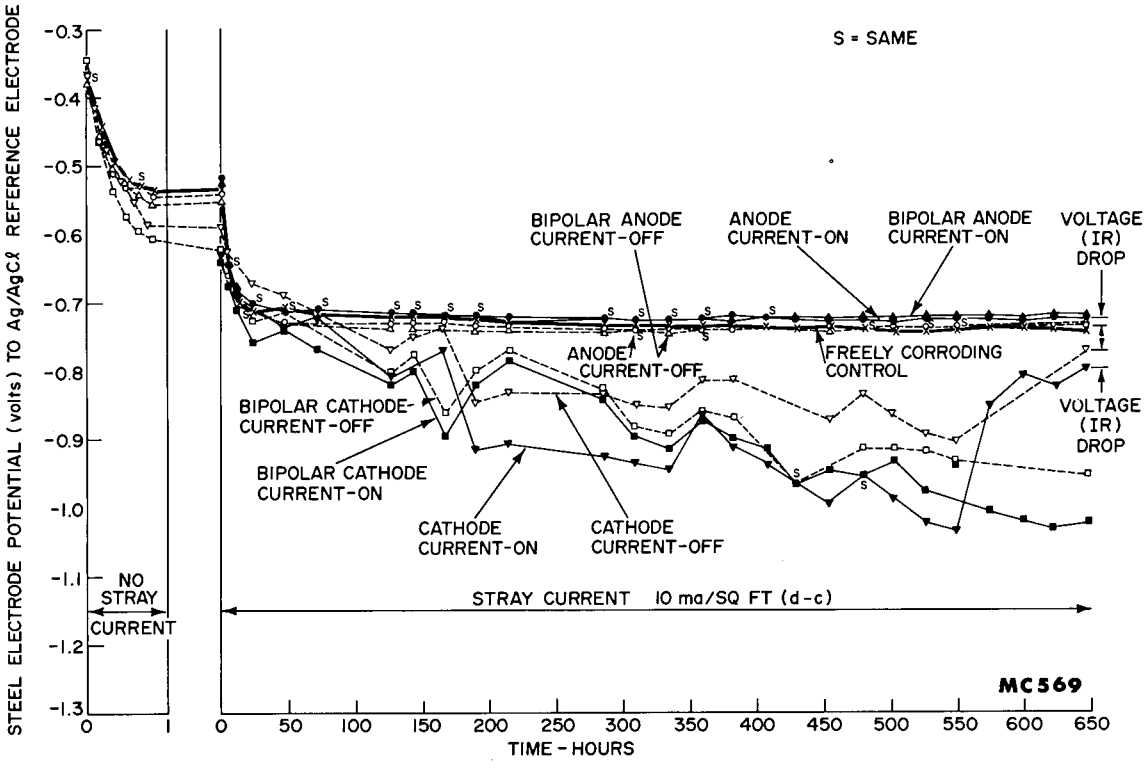


Fig. 4 — The effect of stray direct current on steel electrodes in 0.6M (3.5%) NaCl solution. Potential vs time data at a current density of 10 mA/sq ft.

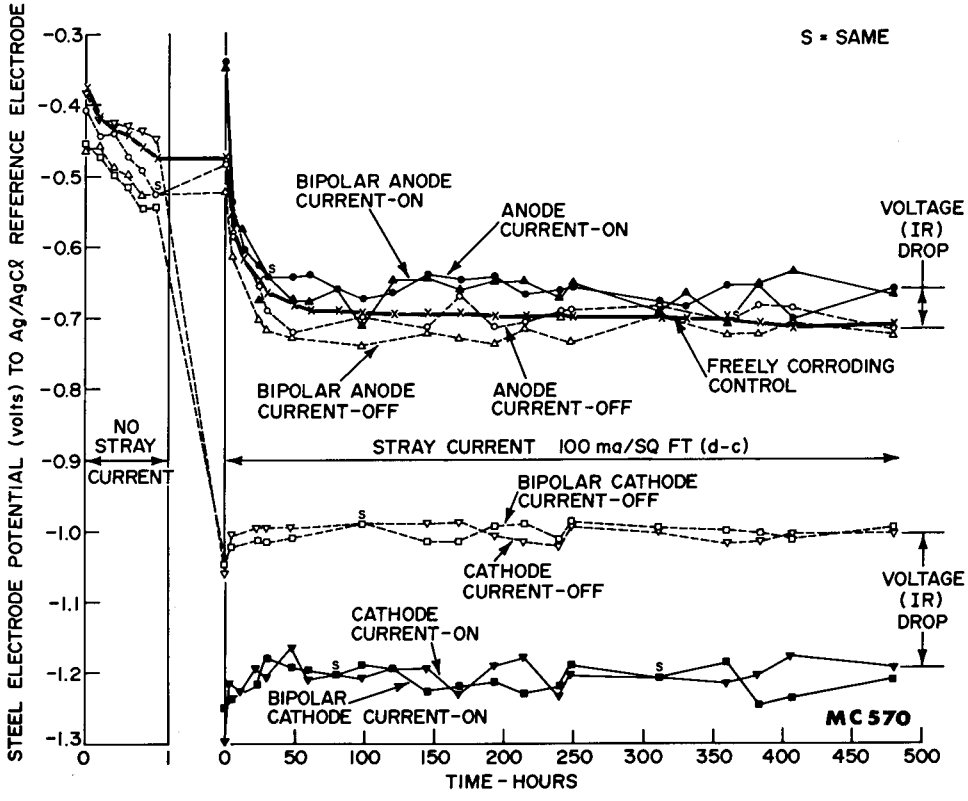


Fig. 5 — The effect of stray direct current on steel electrodes in 0.6M (3.5%) NaCl solution. Potential vs time data at a current density of 100 mA/sq ft.

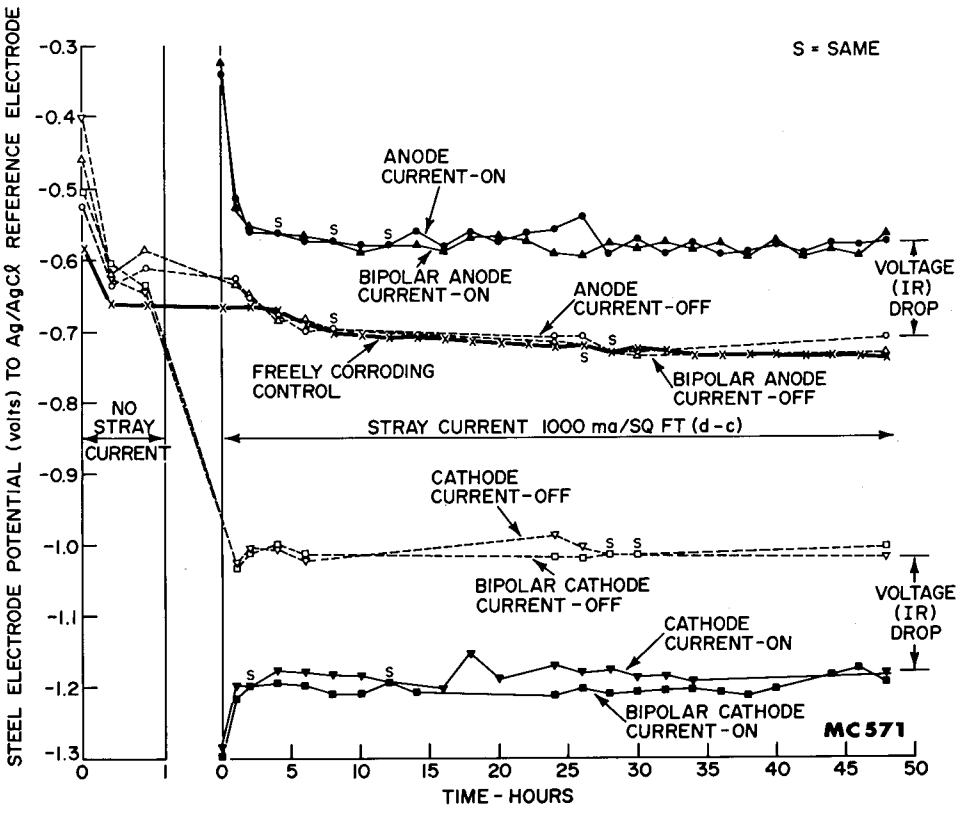


Fig. 6 — The effect of stray direct current on steel electrode in 0.6M (3.5%) NaCl solution. Potential vs time data at a current density of 1000 mA/sq ft.

There was less than a 0.020-V potential difference between the freely corroding specimens, the anodes and bipolar anodes that were corroding, and the cathodes and bipolar cathodes which should be at least partially protected. These small differences in potential were evident even when the potential measurement was made with the current on, i.e., any IR drop was included in the measurement.

Figure 4 shows the potential as a function of time for steel electrodes at a stray dc density of 10 mA/sq ft. As in the case at a current density of 5 mA/sq ft, the potentials for the anodes and bipolar anodes at a current density of 10 mA/sq ft are similar to the freely corroding potentials. Therefore, stray direct currents at a current density of 10 mA/sq ft still could not be detected from potential measurements even if the current interrupter technique was used, i.e., by comparing the current-off to the current-on potential.

At a current density of 10 mA/sq ft, definite potential changes with time occurred on both the cathode and bipolar cathode. These potential changes show that both the cathode and bipolar cathode were being protected because the specimens had polarized to a potential more negative than —0.8 V to the Ag/AgCl reference electrode after

approximately 175 hr. However, these cathodic potential changes could not be used to detect stray currents because they are similar to the potential changes that would be obtained from intentionally applied cathodic protection.

Figure 5 shows that, at a stray dc density of 100 mA/sq ft, an appreciable IR drop exists in the electrode potentials measured at both the anodes and the bipolar anodes of steel. Therefore, if current-on and current-off potential measurements can be made, the existence of stray currents of this current density can be detected from the potential observed. Even if current-on and current-off potential measurements could not be made, the existence of stray currents of this magnitude could be detected by comparing the potential of the bipolar anode with the potential of the same steel in the freely corroding condition. This is possible because a potential difference of approximately 0.05 V would exist. Surges of stray direct currents with a current density of 100 mA/sq ft could also be detected by continuously recording the potential over a period of several days.

Figure 5 also shows that both the cathode and the bipolar cathode polarized to a potential of approximately −1.0 V to the Ag/AgCl reference electrode when the current density was 100 mA/sq ft. This degree of polarization, a change in potential from −0.7 V for the freely corroding specimen to −1.0 V for the cathode and bipolar cathode, also indicates that the cathodes were completely protected. The existence of a stray dc density of 100 mA/sq ft could perhaps be inferred from the extremely negative potentials although a cathodic protection system could also produce negative potentials in the same range. If the current from the cathodic protection system was turned off and the potential remained at extremely negative values over a portion of the hull, the existence of stray currents would be definitely indicated.

Figure 6 shows that with a stray dc density of 1000 mA/sq ft a sizeable IR drop exists at all the steel electrodes. The potentials of the anodes and bipolar anodes with the current on is sufficiently distinct from the freely corroding potential of low-carbon steel that stray currents at a density of 1000 mA/sq ft can be readily detected from potential measurements. The stray current in this instance could be detected either by a direct comparison of the current-on potential to the freely corroding potential or by continuously recording the potential to observe any changes that would be caused by current surges.

At all the stray dc densities studied, the potentials of the anodes and bipolar anodes measured with the current off were essentially identical to the freely corroding potential of low-carbon steel. This indicates that steel does not show appreciable anodic polarization even at a current density of 1000 mA/sq ft. Any anodic potential change observed on steel in 0.6M (3.5%) NaCl solution was a result of an IR drop in the measurement due to the flow of electrical current through the solution.

The potential data for low-carbon steel also indicates that steel cannot be cathodically polarized more negatively than approximately −1.06 V to the Ag/AgCl reference electrode in 0.6M (3.5%) NaCl solution. Cathode potential measurements more negative than −1.06 V can be observed only if a large IR drop is included in the potential measurement.

The significance of the limits of the range of potentials that steel will assume is that the more positive value (approximately −0.7 V) is the potential at which steel will corrode. Regardless of the current density, the potential under anodic conditions (i.e., when steel is dissolving) will remain essentially constant until all the steel has dissolved. The most negative potential (approximately −1.06 V) apparently is the potential at which hydrogen is discharged at both the cathode and bipolar cathode. Potentials this negative, if caused by a cathodic protection system, would indicate that a substantial amount of current is being wasted.

### Steel Metal Loss vs Mean Electrode Potential

Figure 7 shows the steel metal loss in mils per year (mpy) as a function of the mean potential for each type of electrode in the presence or absence of stray direct currents. The mean potential of the anodes and bipolar anodes with the current off was approximately −0.7 V to the Ag/AgCl reference electrode regardless of the anodic current density. However, when the IR drop at the higher current density levels is included in the potential measurement, potential values more positive than −0.7 V were observed.

The mean potentials of the anodes and bipolar anodes at the low current densities were similar to each other and to the mean potential of the freely corroding control specimens. This was true whether the potential measurements were made with the current on or current off. Even without a noticeable change in the mean potential of the anodes and bipolar anodes, a stray dc density of 5 mA/sq ft increased the metal loss rate from 3 to 5 mpy. A current density of 10 mA/sq ft increased the metal loss rate from 3 to 8 mpy. Increases in corrosion of this magnitude would not be catastrophic, but would decrease the life of the steel proportionately.

The metal-loss rate for steel anodes and bipolar anodes was 50 mpy at a current density of 100 mA/sq ft, and approximately 500 mpy at a current density of 1000 mA/sq ft. In both instances the current-off electrode potentials were −0.7 V. Metal loss rates of 50 and 500 mpy would be catastrophic.

Figure 7 also shows that a current density of 5 mA/sq ft was not sufficient to cause any apparent polarization on either the cathodes or bipolar cathodes. This magnitude of current density, however, reduced the rate of steel metal loss from 3 to 1.6 mpy on the bipolar cathode. A current density of 10 mA/sq ft or higher was sufficient to produce significant cathodic polarization and to eliminate essentially all the corrosion on the steel cathodes and bipolar cathodes.

Increase in metal-loss rates at the anodes or bipolar anodes was accompanied by a reduction in the corrosion on the cathodes and bipolar cathodes. This effect would not be practically beneficial, however, because the anodes and bipolar anodes corroded at an accelerated rate.

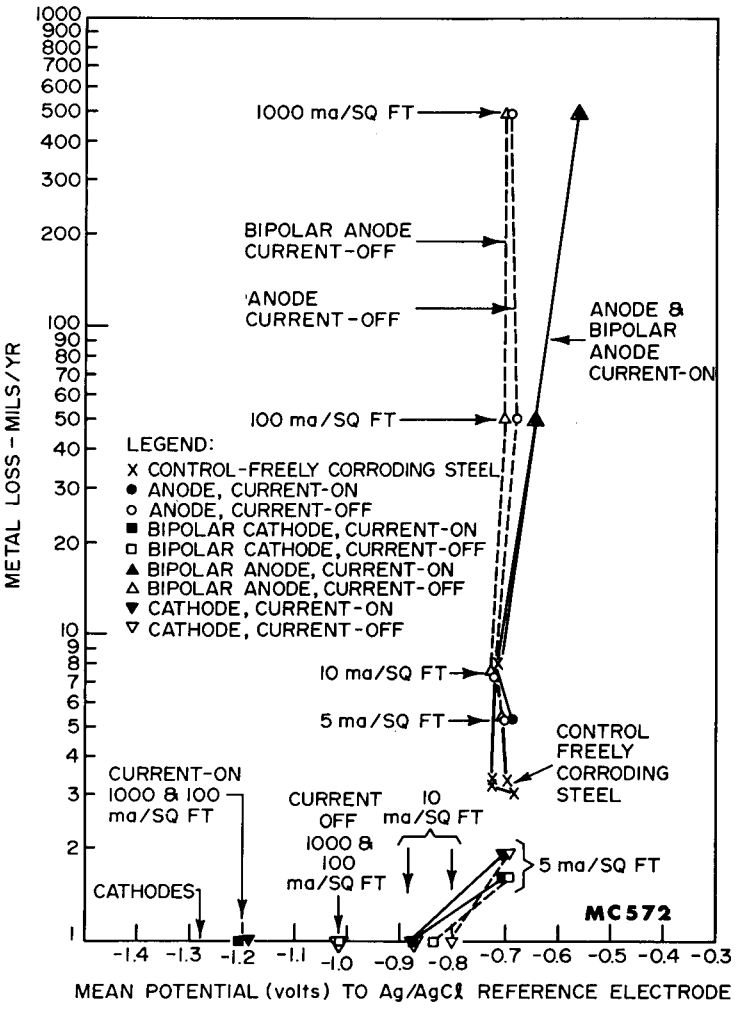


Fig. 7 — Steel metal loss vs mean potential to Ag/AgCl reference electrode in the presence of stray direct current in 0.6M (3.5%) NaCl solution.

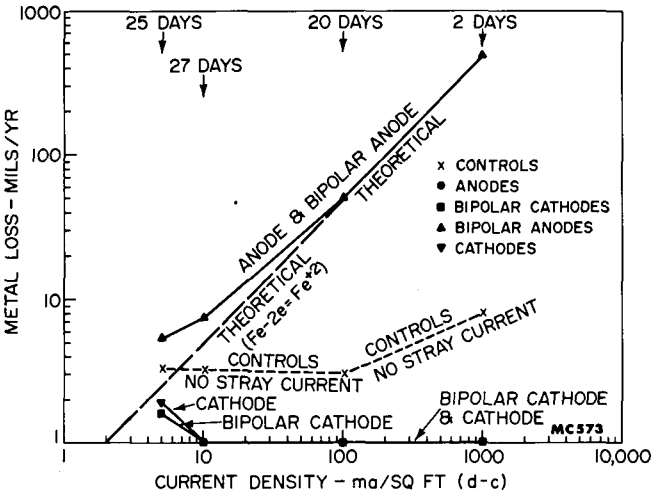


Fig. 8 — Steel metal loss vs current density in the presence of stray direct current in 0.6M (3.5%) NaCl solution

## Steel Metal Loss vs Current Density

Figure 8 shows the theoretical values of steel metal loss in mpy as a function of current density. Data for anodes, bipolar anodes, cathodes, bipolar cathodes and freely corroding control specimens are included in Fig. 8.

The anodes and bipolar anodes at a current density of 100 and 1000 mA/sq ft had a metal-loss rate that was equivalent to the theoretical values for the reaction $Fe—2e=Fe^{+2}$. At a current density of 10 mA/sq ft and less, the metal-loss rates of the anodes and bipolar anodes increased compared to the theoretical values. At a current density of 5 mA/sq ft, the metal-loss rate was approximately 100% greater than the theoretical and 60% greater than for the freely corroding steel.

A stray current density of 100 mA/sq ft increased the metal-loss rate by more than an order of magnitude compared to the freely corroding control exposed for the same time period. A stray current density of 1000 mA/sq ft caused a metal-loss rate increase of almost 2 orders of magnitude compared to the control exposed for the same time period. This latter increase in corrosion is conservative because it is based on control specimens that were exposed for only 2 days; the duration of the experiment at this current density. The metal-loss rate of the control specimens in the 2-day experiment was high compared to the longer term experiments. The high metal loss rate for the freely corroding steel in the shorter term experiments is not uncommon as will be discussed later in this report. Based on the metal-loss rate of the controls in the longer term experiments, steel at a current density of 1000 mA/sq ft would have a metal-loss rate approximately 2-1/2 orders of magnitude greater than the control.

The metal-loss rate is essentially reduced to zero when the current density on either a steel cathode or a bipolar steel cathode is 10 mA/sq ft or greater.

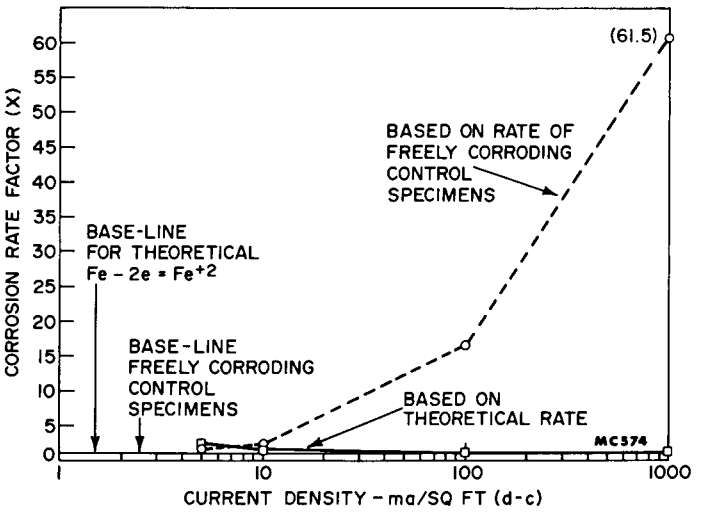


Fig. 9 — Corrosion rate factor (X) vs stray direct-current density for anodes and bipolar anodes of steel

## Corrosion Rate Factor vs Current Density

Figure 9 shows corrosion-rate factors for steel anodes and bipolar anodes as a function of current density. Data have been shown for corrosion-rate factors based on both the theoretical rates and on the rates for freely corroding control specimens. As an example in the use of this graph, at a dc density of 100 mA/sq ft, steel anodes and bipolar anodes would have a corrosion-rate factor of 1 based on the theoretical corrosion rate. Therefore, the corrosion rate would be equivalent to the theoretical. Based on the freely corroding control specimens, the corrosion-rate factor for the steel anodes and bipolar anodes would be approximately 16.5 at a current density of 100 mA/sq ft. Therefore, if a freely corroding specimen had a corrosion rate of 3 mpy, the corrosion rate of the steel anodes and bipolar anodes would be 3 X 16.5 = 49.5 mpy at a current density of 100 mA/sq ft.

A graph of this type is a useful guide in estimating the increased amount of corrosion that could be expected on steel in 0.6M (3.5%) NaCl solution. Similar graphs developed for other metals and other environments would be useful in estimating the increased corrosion that could be expected from stray direct currents.

## Percent Reduction in Corrosion Rate vs Current Density

Figure 10 shows the percent reduction in corrosion rates for steel cathodes and bipolar cathodes as a function of current density. Both the cathodes and bipolar cathodes showed approximately the same percentage reduction in corrosion rates at a particular current density. This was especially true at current densities of 10 mA/sq ft and above, where essentially complete protection was obtained. At a current density of

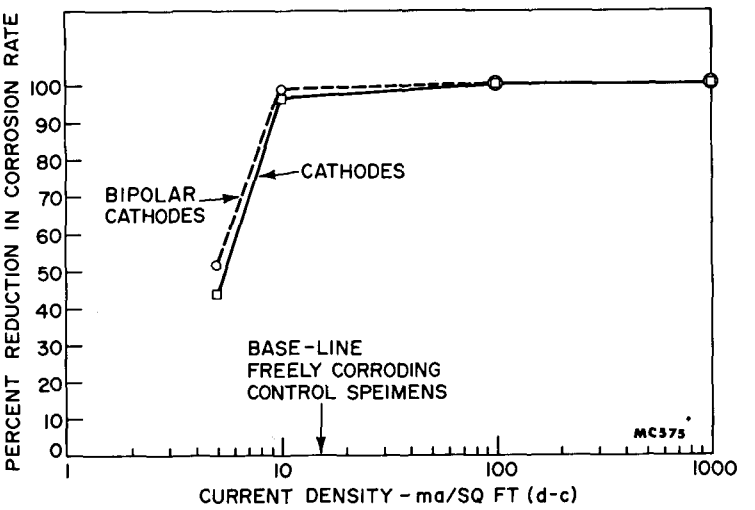


Fig. 10 — Percent reduction in corrosion rate vs stray direct current density for cathodes and bipolar cathodes of steel

5 mA/sq ft, the reduction in corrosion rate was 44% for the cathode and 52% for the bipolar cathode. As discussed earlier, these reductions in corrosion rate occurred without any detectable potential changes.

## Corrosion Rates, Potential Data, and Corrosion Characteristics

Tables 1, 2, and 3 each summarize the corrosion rates, mean electrode potentials and corrosion characteristics for low-carbon steel at various dc densities and in the absence of stray current.

Table 1 shows data for the freely corroding control specimens in the absence of stray currents. The corrosion rate on these specimens ranged from approximately 3 to 8 mpy. With an exposure time of 20 days or more, the corrosion rate was relatively constant at approximately 3 mpy. At the shorter exposure time of 2 days the corrosion rate was approximately 8 mpy. The relatively high corrosion rate in the short exposure time is not unexpected. It is generally agreed that the corrosion rate of unprotected steel decreases with exposure time. The reason for this is that apparently a partially protective film develops on corroding steel with time. The longer term rate is, therefore, lower than the rate in the shorter term experiments where the protective film has not had sufficient time to develop.

The mean electrode potential for the freely corroding steel specimens varied from −0.680 V to −0.726 V in these experiments that ranged from 2 days to 27 days duration. The mean potential of the freely corroding specimens for the four time periods was −0.704 V. For any one time period, the mean potential was within ±0.025 V of this value. The range of potentials were between −0.421 and −0.747 V. The least negative potentials were

observed in the early stages of the experiments, before the steel specimens had stabilized in the environment, and therefore are not indicative of the actual electrode potentials.

General corrosion was observed on all the freely corroding steel specimens. On some specimens the corrosion was relatively uniform while on others the corrosion occurred on approximately 75% of the exposed area.

Table 2 shows the data for the anodes and the bipolar anodes of low-carbon steel in the presence of stray direct currents. The corrosion rates for the anodes and bipolar anodes were essentially the same at any one current density. The corrosion rates ranged from 5.3 mpy at a current density of 5 mA/sq ft to 492 mpy at a current density of 1000 mA/sq ft.

The mean potentials for all the time periods measured with the current off (IR drop excluded from the measurement) was −0.700 V for the steel anodes and −0.709 V for the bipolar anodes. This difference cannot be considered a real difference in potential because for both the anodes and bipolar anodes the mean potentials varied by more than 0.01 V from one current density to another. However, the mean potentials of all the anodes and bipolar anodes measured with the current off were within ±0.005 V of the freely corroding mean potential (compare Tables 1 and 2).

Table 1
Corrosion Rates, Potential Data and Corrosion Characteristics for Low Carbon Steel Controls: No Stray Current; Freely Corroding in 0.6M (3.5%) NaCl Solution

| Controls For Current Density at mA/sq ft Shown | Test Duration (days) | Corrosion Rate (mpy*) | Potential† | | | | Corrosion Characteristics |
|---|---|---|---|---|---|---|---|
| | | | Mean | | Range | | |
| | | | Current On | Current Off | Current On | Current Off | |
| 1000 | 2 | 8.1 | — | −0.714 | — | −0.666 to −0.738 | General and relatively uniform corrosion |
| 100 | 20 | 3.1 | — | −0.680 | — | −0.473 to −0.730 | General and relatively uniform corrosion |
| 10 | 27 | 3.2 | — | −0.726 | — | −0.534 to −0.746 | General corrosion on 75% of exposed area |
| 5 | 25 | 3.3 | — | −0.696 | — | −0.421 to −0.747 | General corrosion on 75% of exposed area |
| | | | Mean = | −0.704 | | | |

*mpy = mils penetration per year, 1 mil = 0.001 in.
†Potentials measured to Ag/AgCl reference electrode.

Table 2
Corrosion Rates, Potential Data and Corrosion Characteristics for Low Carbon Steel: Anodes and Bipolar Anodes; Stray Direct Currents Present in 0.6M (3.5%) NaCl Solution

| Current Density (mA/sq ft) | Test Duration (days) | Corrosion Rate (mpy*) | Potential† | | | | Corrosion Characteristics |
|---|---|---|---|---|---|---|---|
| | | | Mean | | Range | | |
| | | | Current On | Current Off | Current On | Current Off | |
| Anode | | | | | | | |
| 1000 | 2 | 491 | −0.563 | −0.694 | −0.340 to −0.594 | −0.628 to −0.730 | Channeled by corrosion at tape edges; uniform corrosion other areas |
| 100 | 20 | 50 | −0.642 | −0.678 | −0.339 to −0.702 | −0.483 to −0.722 | Very sharp corroded channels at some locations of taped edges; some areas uncorroded or very small amount of corrosion |
| 10 | 27 | 7.3 | −0.714 | −0.724 | −0.518 to −0.730 | −0.538 to −0.741 | General corrosion entire exposed areas and some areas under tape |
| 5 | 25 | 5.3 | −0.690 | −0.705 Mean = −0.700 | −0.489 to −0.736 | −0.527 to −0.742 | General corrosion entire exposed area |
| Bipolar Anode | | | | | | | |
| 1000 | 2 | 492 | −0.567 | −0.699 | −0.323 to −0.595 | −0.633 to −0.734 | Channeled by corrosion at tape edges; uniform corrosion other areas |
| 100 | 20 | 50 | −0.643 | −0.699 | −0.347 to −0.710 | −0.520 to −0.741 | Channeled by corrosion at some location of taped edges; some areas uncorroded or very small amount of corrosion |
| 10 | 27 | 7.6 | −0.714 | −0.726 | −0.528 to −0.728 | −0.550 to −0.745 | General corrosion entire exposed area |
| 5 | 25 | 5.4 | −0.702 | −0.710 Mean = −0.709 | −0.547 to −0.741 | −0.563 to −0.748 | General corrosion entire exposed area |

*mpy = mils penetration per year, 1 mil = 0.001 in.
†Potentials measured to Ag/AgCl reference electrode.

Table 3
Corrosion Rates, Potential Data and Corrosion Characteristics for Low Carbon Steel: Cathodes and Bipolar Cathodes; Stray Direct Currents Present in 0.6M (3.5%) NaCl Solution

| Current Density (mA/sq ft) | Test Duration (days) | Corrosion Rate (mpy*) | Potential† | | | | Corrosion Characteristics |
|---|---|---|---|---|---|---|---|
| | | | Mean | | Range | | |
| | | | Current On | Current Off | Current On | Current Off | |
| Cathode | | | | | | | |
| 1000 | 2 | 0 | −1.190 | −1.011 | −1.152 to −1.284 | −0.987 to −1.028 | No corrosion but some small areas with peened appearance |
| 100 | 20 | 0 | −1.208 | −1.010 | −1.154 to −1.325 | −0.988 to −1.059 | No corrosion |
| 10 | 27 | 0.12 | −0.872 | −0.802 | −0.602 to −1.034 | −0.556 to −0.904 | Slight general corrosion on <10% of exposed area |
| 5 | 25 | 1.9 | −0.705 | −0.694 | −0.595 to −0.760 | −0.577 to −0.757 | General corrosion on 35-40% of exposed area |
| Bipolar Cathode | | | | | | | |
| 1000 | 2 | 0 | −1.207 | −1.015 | −1.175 to −1.314 | −1.001 to −1.033 | No corrosion but some small areas with peened appearance |
| 100 | 20 | 0 | −1.211 | −1.014 | −1.178 to −1.250 | −0.987 to −1.047 | No corrosion |
| 10 | 27 | 0.04 | −0.873 | −0.836 | −0.629 to −1.041 | −0.607 to −0.978 | Slight general corrosion on <10% of exposed area |
| 5 | 25 | 1.6 | −0.703 | −0.694 | −0.592 to −0.758 | −0.524 to −0.756 | General corrosion on 45-50% of exposed area |

*mpy = mils penetration per year, 1 mil = 0.001 in.
†Potentials measured to Ag/AgCl reference electrode.

The mean potentials in Table 2 also show that at current densities of 5 and 10 mA/sq ft, there was less than 0.015 V difference between the current-on and the current-off potentials for both the anodes and bipolar anodes. The existence of stray current could not be readily detected from current-on and current-off potential measurements at these current densities because of the small IR drop. At current densities of 100 and 1000 mA/sq ft, sufficient IR drop was evident so that stray currents could be readily detected from current-on and current-off potential measurements. The range of potentials for the anodes and bipolar anodes were similar when the current-on and current-off potentials are viewed at a particular current density.

The corrosion characteristics of steel anodes and bipolar anodes were similar at any one current density. At current densities of 5 and 10 mA/sq ft, general corrosion was evident over the entire exposed areas. At current densities of 100 and 1000 mA/sq ft, very accelerated corrosion was evident at the edges of the tape used to mask certain areas from the solution. This corrosion occurred in the form of deep channels. At a current density of 1000 mA/sq ft, this type corrosion occurred along all the tape edges, but at a current density of 100 mA/sq ft occurred only at some locations along the tape. The areas distant from the tape edges were uniformly corroded at a current density of 1000 mA/sq ft, but at a current density of 100 mA/sq ft, some areas away from the tape were essentially uncorroded.

Table 3 shows the summary data for the cathodes and bipolar cathodes of steel in the presence of stray direct currents. The corrosion rate at any one current density is similar for the cathode and bipolar cathode except at a current density of 10 mA/sq ft. At this current density, the bipolar cathode had a lower corrosion rate than the cathode. The lower corrosion rate for the bipolar cathode in this instance was undoubtedly the result of the bipolar cathode being slightly more polarized than the cathode. This additional polarization was indicated by the mean current-off potential measurements; −0.802 V for the cathode and −0.836 V for the bipolar cathode. As noted earlier, at a current density of 5 mA/sq ft the corrosion rate of both the cathode and bipolar cathode was reduced approximately 50% compared to the freely corroding control specimen, although no noticeable polarization of these electrodes was evident from the electrode potential measurements.

Current densities above 5 mA/sq ft caused varying degrees of cathodic polarization. The mean current-off potentials show that for both the cathodes and bipolar cathodes −1.015 V was the most negative mean potential to which steel cathodes could be polarized in 0.6M (3.5%) NaCl solution. More negative mean potentials were not true polarization potentials because the value included an IR drop.

The change to more negative potentials shown by the ranges of potentials for both the cathodes and bipolar cathodes with the current off and above a current density of 10 mA/sq ft is indicative of cathodic polarization. At a current density of 100 mA/sq ft and above, polarization of the cathodes and bipolar cathodes occurred almost immediately on applying the current. The immediate cathodic polarization at these high current densities was evident from the instantaneous current-off potentials which were approximately −1 V (Figs. 5 and 6).

The corrosion characteristics of the cathodes and the bipolar cathodes were the same at any one current density. As expected, no corrosion occurred at current densities of 100 and 1000 mA/sq ft, although at the latter current density some small areas had a peened appearance. The cathode and bipolar cathode at a current density of 10 mA/sq ft had only slight general corrosion on less than 10% of the exposed area, and the corrosion rate had been reduced by more than 96% (Fig. 10). At a current density of 5 mA/sq ft, general corrosion occurred on 35 to 40% of the exposed area of the cathode and 45 to 50% of the exposed area of the bipolar cathode.

## CONCLUSIONS

1. An experimental technique has been developed which makes it possible to individualize bipolar anodes and bipolar cathodes so that stray-current corrosion parameters can be studied and quantized.

2. Low-carbon steel had a mean potential range of from −0.700 V to −1.015 V to the Ag/AgCl reference electrode in 0.6M (3.5%) NaCl solution under the conditions of these experiments. The least negative potential was measured on anodes, bipolar anodes and freely corroding control specimens. Regardless of the anode current density, steel corroded at a potential of approximately −0.7 V. Any more positive potential measured on steel was caused by an IR drop in the potential measurement as a result of the dc flow through the solution. The most negative potential was the potential to which steel was polarized cathodically. The most negative potential with the current off is undoubtedly the potential at which the only cathodic reaction occurring is hydrogen discharge. A mean potential more negative than −1.015 V to the Ag/AgCl reference electrode was obtained only when the measurement included an IR drop.

3. At stray dc densities of 5 and 10 mA/sq ft on steel, the IR drop was too small to detect stray currents from potential measurements.

4. Stray direct-current densities of 100 and 1000 mA/sq ft were readily detected from potential measurements because there was an appreciable IR drop at the bipolar anodes. The stray currents of this magnitude were detectable by either measuring the potential changes that occurred with the current on and the current off or by comparing the potentials measured with the current on to the potentials of the freely corroding control specimens.

5. The metal-loss rate for steel anodes and bipolar anodes was 50 mpy at a current density of 100 mA/sq ft and approximately 500 mpy at a current density of 1000 mA/sq ft. These increases in metal-loss rate would be catastrophic.

6. Even without a noticeable potential change at the anodes and bipolar anodes of steel, a stray direct current of 10 mA/sq ft increased the metal-loss rate from 3 to 8 mpy. This increase in metal-loss rate would not be catastrophic but would proportionately shorten the life of the steel.

7. A current density of 5 mA/sq ft was not sufficient to cause any apparent cathodic polarization, but reduced the metal-loss rate by approximately 50%. A current density of 10 mA/sq ft produced significant cathodic polarization and essentially eliminated corrosion on the steel cathodes and bipolar cathodes.

8. The anodes and bipolar anodes at current densities of 100 and 1000 mA/sq ft had a metal-loss rate equivalent to the theoretical values for the reaction $Fe-2e=Fe^{+2}$. At current densities of 5 and 10 mA/sq ft, the metal-loss rates increased compared to the theoretical values.

9. General corrosion was observed on all the freely corroding steel specimens.

10. The corrosion characteristics of steel anodes and bipolar anodes were similar at any one current density. At current densities of 5 and 10 mA/sq ft, general corrosion occurred over the entire exposed areas. At current densities of 100 and 1000 mA/sq ft, highly localized corrosion in the form of deep channels occurred at the edges of the tape used for masking specific areas from the solution. At a current density of 100 mA/sq ft, some areas away from the tape were essentially uncorroded.